Cross–Seasonal Impact of SST Anomalies over the Tropical Central Pacific Ocean on the Antarctic Stratosphere

Yucheng Zi[1,2,3,4], Zhenxia Long[3], Jinyu Sheng[2], Gaopeng Lu[4], Will Perrie[2,3,5], and Ziniu Xiao[1,4]

Correspondence: Zhenxia Long (Zhenxia.Long@dfo-mpo.gc.ca) and Ziniu. Xiao (xiaozn@lasg.iap.ac.cn)

[1] State Key Laboratory of Earth System Numerical Modeling and Application, Institute of Atmospheric Physics, Chinese Academy of Sciences, Beijing, China

[2] Department of Oceanography, Dalhousie University, Halifax, Nova Scotia, Canada

[3] Fisheries and Oceans Canada, Bedford Institute of Oceanography, Dartmouth, Nova Scotia, Canada

[4] School of Earth and Space Sciences, University of Science and Technology of China, Hefei, China

[5] Department of Engineering Mathematics & Internetworking, Dalhousie University, Halifax, Canada

21 November 2025

Abstract

In this study we examine the cross–seasonal effects of boreal winter sea surface temperature (SST) anomalies over the central tropical Pacific (Niño 4 region) on Antarctic stratospheric circulation and ozone transport during the subsequent austral winter using ERA5 reanalysis of 45 years (1980–2024). Our analyses show that warm (cold) SST anomalies in Niño 4 region during December–February are associated with mid- and high-latitude stratospheric warming (cooling), a contracted (expanded) stratospheric polar vortex (SPV), and enhanced (suppressed) polar ozone concentrations during July–September of the subsequent year. This delayed response is mediated by a Pacific–South America (PSA) teleconnection, which excites planetary waves that propagate upward into stratosphere and modify the Brewer–Dobson circulation. In addition, as the influence of Niño 4 SSTs on the PSA teleconnection pattern diminishes during July-September, surface heat feedback at mid and high latitudes becomes critically important for planetary waves. Specifically, persistent South Pacific SST warming and sea-ice loss over the Amundsen and Ross Seas reinforce planetary waves by releasing heat from ocean into atmosphere. A multivariate regression statistical model using factors of boreal winter Niño 4 SST and June PSA indices explain approximately 32 % of the variance in austral winter stratospheric temperatures. These findings highlight a previously underexplored pathway through which tropical Pacific SST anomalies modulate Antarctic stratospheric dynamics on seasonal timescales.

Keywords: El Niño–Southern Oscillation (ENSO); Stratospheric warming; Stratospheric polar vortex (SPV); Pacific–South America (PSA) pattern; Multivariate regression

1 Introduction

The Antarctic stratospheric circulation is largely governed by the wintertime Stratospheric Polar Vortex (SPV), which is a major driver of weather and climate variability across the Southern Hemisphere (Baldwin et al., 2021). Compared to its Northern Hemisphere counterpart, the Antarctic SPV is generally more stable, owing to weaker thermal contrasts between the ocean and land. Despite this stability, the Antarctic SPV exhibits considerable interannual variability (Domeisen et al., 2019; Baldwin et al., 2021). Furthermore, the Antarctic stratosphere plays a crucial role in modulating weather and climate in the Southern Hemisphere through the seasonal evolution of SPV and its dynamics processes and interaction with ozone chemistry (Thompson et al., 2005; Solomon et al., 2016).

Previous studies revealed large interannual variations and long-term trends in the SPV, stratospheric temperatures, and ozone concentrations (Karpetchko et al., 2005). Superimposed on the long-term trends of SPV are substantial interannual variations and extreme events. For instance, exceptionally weak SPV episodes triggered by sudden stratospheric warmings (SSWs) occurred respectively in 2002, 2010, 2019, and 2024 (Thompson and Solomon, 2002; Esler et al., 2006; Laat and Weele 2011; Shen et al., 2020; Zi et al., 2025), and an unusually strong SPV event driven by the pronounced ozone depletion occurred in 2020 (Lim et al., 2024).

Several natural factors contribute to the above-mentioned SPV variability. The phase of the Quasi-Biennial Oscillation (QBO), for instance, modulates planetary-wave propagation and can either strengthen or weaken the SPV (Kuroda et al., 2007). El Niño–Southern Oscillation (ENSO) events also leave distinct warm- and cold-year signatures on Antarctic stratospheric temperatures through changes in tropospheric wave forcing and the Brewer–Dobson (B-D) circulation (Yang et al., 2015; Stone et al., 2022; Rao et al., 2023; Wang et al., 2025). Previous studies also suggest sea ice can have significant impact on the SPV (e.g., Rea et al., 2024; Song et al., 2025; Sun et al., 2015), with implications for Southern Hemisphere climate variability. In addition, solar-cycle variability contributes to interannual modulation by altering ultraviolet irradiance and stratospheric heating rates (Kuroda et al., 2007). Alongside these natural drivers, fluctuations in the atmospheric burdens of ozone-depleting substances and greenhouse gases continue to influence both the magnitude and nature of Antarctic stratospheric variability (Singh and Bhargawa, 2019).

ENSO is the most prominent mode of interannual climate variability (Wang, 2018). Developing in boreal autumn and peaking in winter, ENSO influences the global weather patterns through atmospheric teleconnections (McPhaden et al., 2006). It also modulates the SPV primarily via the Pacific–North America (PNA) and Pacific–South America (PSA) wave trains (Garfinkel and Hartmann, 2008; Ineson and Scaife, 2009; Barriopedro and Calvo, 2014; Polvani et al., 2017; Song and Son, 2018; Zhang et al., 2022). In the Northern Hemisphere, El Niño events enhance tropical convection and amplify the PNA pattern, strengthening the Aleutian Low, which in turn increases upward wave activity and weakens the SPV (Garfinkel and Hartmann, 2008; Butler and Polvani, 2011; Zhang et al., 2022). In the Southern Hemisphere, central Pacific (CP–type) El Niño events during September–February enhance convection near the South Pacific Convergence Zone (SPCZ), which triggers the PSA wave trains that can weaken the Antarctic SPV, resulting in stratospheric warming and ozone enhancement (Hurwitz et al., 2011a,b; Yang et al., 2015; Manatsa and Mukwada, 2017; Domeisen et al., 2019; Ma et al., 2022). In contrast, Eastern Pacific (EP–type) El Niño events were found to produce weaker stratospheric responses (Hurwitz et al., 2011a; Zubiaurre and Calvo, 2012).

Although many studies were made on the Antarctic stratosphere's simultaneous or 1-2 months lag responses to ENSO from September to February (L'Heureux and Thompson, 2006; Silvestri and Vera, 2009; Hu and Fu, 2010; Fogt et al., 2011; Lin et al., 2012; Kim et al., 2017; Ma et al., 2022), our knowledge remains very limited on the ENSO's cross–seasonal and delayed effects (Manatsa and Mukwada, 2017; Niu et al., 2023). Some previous studies found that delayed ozone responses occur in the year following an ENSO event (Lin and Qian, 2019), while others suggested that tropical sea surface temperature (SST) anomalies as early as June can influence stratospheric circulation later in the year (Grassi et al., 2008; Evtushevsky et al., 2015; Lim et al., 2018; Stone et al., 2022). Yang et al. (2015) examined correlations between ENSO and Antarctic stratospheric temperatures during July–September, but these were primarily interpreted as concurrent responses. Despite these studies, the physical mechanisms by which ENSO events in boreal winter influence the Antarctic stratosphere during the following austral winter (July–September) remain poorly understood. Better understanding of ENSO's delayed impact is particularly important, since the SPV in the austral winter is strongest and most susceptible to dynamical disturbances, with significant implications for forecast of Antarctic stratospheric extreme events (Lin et al., 2009; Thompson et al., 2011).

The main objective of this study is to examine how the boreal winter SST anomalies (SSTs) influence the Antarctic stratosphere during the following austral winter, with a special emphasis on mechanisms by which Niño 4 SSTs modulate polar stratospheric dynamics, and associated planetary wave propagation and mid-latitude sea-air interactions. The structure of this paper is as follows. Section 2 describes the data and methodology. Section 3 presents quantification of the ENSO–Antarctic stratosphere relationship. Section 4 shows an examination of the underlying dynamical mechanisms. Section 5 presents the multivariate regression analysis. Section 6 is a summary and conclusion.

2. Data and methods

2.1 Data

The 6-hourly and monthly-mean atmospheric variables in the 45-year period 1980–2024 extracted from the ERA5 reanalysis (Hersbach et al., 2023a,b) are used in this study. This reanalysis with a horizontal resolution of 1°×1° was generated by the European Centre for Medium-Range Weather Forecasts (ECMWF). These atmospheric variables at 37 vertical pressure levels include the geopotential height, horizontal and vertical winds, temperature, sea level pressure (SLP), ozone mass mixing ratio, total column ozone (TCO_3), net surface downward short-wave radiation flux, net surface upward long-wave radiation flux, latent and sensible heat fluxes, outgoing long-wave radiation flux (OLR). The monthly sea surface temperature (SST) and sea-ice concentration (SIC) during the same study period were also extracted from ERA5 reanalysis.

Several indices (such as Niño 3, Niño 3.4, and Niño 4) based on SST anomalies averaged over a given region have been used to monitor the dynamic activities in the tropic Pacific (Bamston et al. 1997; Trenberth, 1997). Niño 3 is the SST anomalies averaged over the region between 5 °N–5 °S and 150 °W–90 °W, and has been used for monitoring and predicting El Niño and La Niña events (Trenberth, 1997). Niño 3.4 is the SST anomalies averaged over the region between 5 °N–5 °S and 170 °W–120 °W, and has been used as the primary index for monitoring ENSO due to its ability to capture basin-scale variability (Bamston et al. 1997). Niño 4 is the SST anomalies averaged over the region between 5 °N–5 °S and 160 °E–150 °W, which is to monitor

SST anomalies in the central equatorial Pacific. In this study, the SST indices for Niño 3, Niño 3.4, and Niño 4 were obtained from the HadISST1.1 dataset (Rayner et al., 2003). Since results obtained after filtering the interannual component are similar, no filtering has been applied.

The Pacific–South America pattern (PSA) index was used to examine stratosphere and troposphere interactions, which was derived by projecting area–weighted SLP anomalies south of 20 °S onto the second Empirical Orthogonal Function (EOF) mode (Mo and Higgins, 1998). All anomalies are calculated relative to the 1991–2020 daily and monthly climatology, and all data have been detrended. Statistical significance is assessed using the Student's t-test.

2.2 Method

2.2.1 E–P flux

The Eliassen–Palm (E–P) theorem is used to diagnose interactions between eddies and the zonal–mean flow in both the stratosphere and troposphere (Andrews et al., 1987). The E–P flux ($\vec{F}$) and its divergence ($\nabla \cdot \vec{F}$) are defined:

$$\vec{F} = \left(\vec{F}_{\varphi}, \vec{F}_{p}\right) = r_0 cos\varphi \left\{-\left[u'v'\right], \frac{f}{\left[\theta_p\right]}\left[v'\theta'\right]\right\} \tag{1}$$

$$\nabla \cdot \vec{F} = \frac{1}{r_0 \cos\varphi}\frac{\partial}{\partial\varphi}\left(\vec{F}_{\varphi} \cos\varphi\right) + \frac{\partial}{\partial p}\left(\vec{F}_{p}\right) \tag{2}$$

where u and v are the zonal and meridional wind components, respectively, and θ is the potential temperature. φ and p denote latitude and pressure, respectively. f is the Coriolis parameter, and r_0 is Earth's radius. Square brackets [ ] indicate zonal averages, and primes (′) denote deviations from the zonal mean.

2.2.2 Takaya–Nakamura (TN01) wave activity flux

The Takaya-Nakamura (2001) wave activity flux (TN01 flux) has been used for determining the horizontal propagation of quasi-stationary Rossby waves in a zonally varying background flow (Takaya and Nakamura, 2001). The zonal (F_x) and meridional (F_y) components of TN01 are defined as:

$$F_x = \frac{p}{2|U^{*}|{r_0}^2}\left(\frac{U}{cos\,\varphi}\left(\left(\frac{\partial\psi'}{\partial\lambda}\right)^2 - \psi'\frac{\partial^2\psi'}{\partial\lambda^2}\right) + V\left(\frac{\partial\psi'}{\partial\lambda}\frac{\partial\psi'}{\partial\varphi} - \psi'\frac{\partial^2\psi'}{\partial\lambda\partial\varphi}\right)\right) \quad (3)$$

$$F_y = \frac{p}{2|U^{\times}|{r_0}^2}\left(U\left(\frac{\partial\psi'}{\partial\lambda}\frac{\partial\psi'}{\partial\varphi} - \psi'\frac{\partial^2\psi'}{\partial\lambda\partial\varphi}\right) + V\,cos\,\varphi\left(\left(\frac{\partial\psi'}{\partial\varphi}\right)^2 - \psi'\frac{\partial^2\psi'}{\partial\varphi^2}\right)\right) \quad (4)$$

where ψ represents the stream function, λ and φ denote longitude and latitude, respectively, and $|U^{\times}|$ is the magnitude of the total horizontal wind velocity. U and V are the climatological mean zonal and meridional wind components, respectively, while p is pressure, and r_0 is Earth's radius.

2.2.3 Residual mean meridional circulation

The Transformed Eulerian–Mean (TEM) formulation suggested by Andrews and McIntyre (1976, 1978) has widely been employed for diagnosing the large–scale circulation in the middle atmosphere. Different from the conventional Eulerian mean, the TEM framework accounts for eddy heat and momentum fluxes, thereby providing a more accurate representation of actual mass transport. In particular, the residual mean meridional circulation encapsulates the net effect of both mean flow and wave–induced eddy motions, making it especially useful for diagnosing stratospheric processes, such as B-D circulation and wave–driven anomalies associated with stratospheric warming. It is defined as:

$$[v]^{*} = [v] - \frac{1}{\rho_0}\frac{\partial}{\partial z}\left(\frac{\rho_0\,[v'\theta']}{[\theta_z]}\right) \quad (5)$$

$$[w]^{*} = [w] - \frac{1}{r_0\,cos\,\varphi}\frac{\partial}{\partial\varphi}\left(\frac{cos\,\varphi\,[v'\theta']}{[\theta_z]}\right) \quad (6)$$

where $[v]^{*}$ and $[w]^{*}$ denote the meridional and vertical components of the residual velocity, respectively. The vertical coordinate z is the log-pressure height defined as $z = -H\,log\frac{p}{1000\,hPa}$, where H is the scale height (≈ 7 km). All other variables are consistent with those defined in Equations (1)–(4).

2.2.4 Residual mean meridional circulation

The quasi-geostrophic wave refraction index (n^2) is also employed to diagnose the propagation characteristics of planetary waves (O'Neill and Youngblut, 1982). In general, planetary waves tend to propagate toward regions with a larger value of the refraction index. The formula is given as follows:

$$n^2 = [\frac{\bar{q}_\varphi}{r_0(\bar{u} - c)} - \left(\frac{k}{r_0 \cos\varphi}\right)^2 - \left(\frac{f}{2NH}\right)^2]{r_0}^2 \tag{7}$$

where the meridional gradient of the zonal mean potential vorticity $\bar{q}_\varphi$ is (Albers and Birner, 2014):

$$\bar{q}_\varphi = 2\Omega\cos\varphi - \left[\frac{(\bar{u}\cos\varphi)_\varphi}{r_0\cos\varphi}\right]_\varphi + \frac{r_0 f^2}{R_d}\left(\frac{p\theta}{T}\frac{\overline{u_p}}{\overline{\theta_p}}\right)_p \tag{8}$$

Where u is the zonal-mean zonal wind; $N, H,$ $k,$ f, φ r_0 rand Ω are the buoyancy frequency, scale height, zonal wave number, the Coriolis parameter, latitude, Earth’s radius and angular frequency of Earth, respectively. The subscripts refer to derivatives with respect to the given variable and the prime denotes the departure from the zonal mean.

2.2.5 CMIP6 datasets

To validate the observational results with model simulations, output from Phase 6 of the Coupled Model Intercomparison Project (CMIP6) are examined. Historical simulations were performed using fully coupled atmosphere–ocean models forced with observed external drivers, including greenhouse gases, aerosols, volcanic eruptions, and solar variability. The analysis focuses on monthly mean SST, SIC, and temperature at 10 hPa over the period 1951–2014. A total of 20 fully coupled CMIP6 models are included: CESM2, CESM2-FV2, CESM2-WACCM, CESM2-WACCM-FV2, EC-Earth3-AerChem, EC-Earth3-Veg, EC-Earth3-CC, GISS-E2-1-G, MPI-ESM-1-2-HAM, MPI-ESM1-2-LR, E3SM-1-0, E3SM-1-1-ECA, ACCESS-CM2, HadGEM3-GC31-LL, BCC-CSM2-MR, CanESM5-1, CAS-ESM2-0, CIESM, FIO-ESM-2-0, SAM0-UNICON. Because these selected CMIP6 models differ in their horizontal resolutions, to ensure consistency across datasets, all fields are interpolated onto a uniform 1°×1° latitude–longitude grid to ensure consistency across datasets.

3 Impacts of ENSO on stratospheric atmospheric circulation

To quantify the cross–seasonal response of the Antarctic stratospheric circulation to ENSO, we first correlate three ENSO indices: Niño 4, Niño 3.4, and Niño 3, with the stratospheric temperature (T_{10-30}) and zonal wind (U_{10-30}) over Antarctica during the subsequent July–September period. Here, T_{10-30} refers to the zonal-mean temperature averaged over 60 °S–90 °S at 10–30 hPa, and U_{10-30} refers to the zonal-mean zonal wind averaged over 40 °S–50 °S at the same pressure levels (Table 1).

Table 1. Correlation coefficients between Niño 4, Niño 3.4 and Niño 3 indices and zonal-mean temperature index (T_{10-30}) averaged over 60 °S to 90 °S as well as zonal wind index (U_{10-30}) averaged over 40 °S to 50 °S at 10–30 hPa.

	T_{10-30}_Jul	T_{10-30}_Aug	T_{10-30}_Sep	U_{10-30}_Jul	U_{10-30}_Aug	U_{10-30}_Sep
Niño 4_Sep	0.37***	0.36**	0.32**	-0.26*	-0.31**	-0.30**
Niño 4_Oct	0.35**	0.36**	0.34**	-0.22	-0.29*	-0.32**
Niño 4_Nov	0.37***	0.40***	0.32**	-0.22	-0.32**	-0.31**
Niño 4_Dec	0.38***	0.42***	0.35**	-0.24	-0.37***	-0.34**
Niño 4_Jan	0.42***	0.43***	0.30**	-0.31**	-0.40***	-0.33**
Niño 4_Feb	0.41***	0.41***	0.31**	-0.30**	-0.38***	-0.32**
Niño 4_Mar	0.38***	0.39***	0.30**	-0.23	-0.34**	-0.28*
Niño 3.4_Sep	0.34**	0.26*	0.20	-0.20	-0.21	-0.20
Niño 3.4_Oct	0.32**	0.27*	0.24	-0.19	-0.21	-0.23
Niño 3.4_Nov	0.34**	0.29*	0.23	-0.20	-0.23	-0.23
Niño 3.4_Dec	0.37***	0.31**	0.25*	-0.19	-0.24	-0.23
Niño 3.4_Jan	0.38***	0.32**	0.21	-0.24	-0.26*	-0.21
Niño 3.4_Feb	0.38***	0.32**	0.21	-0.25*	-0.26*	-0.21
Niño 3.4_Mar	0.36**	0.35**	0.25*	-0.23	-0.28*	-0.23
Niño 3_Sep	0.33**	0.22	0.14	-0.18	-0.17	-0.16
Niño 3_Oct	0.31**	0.21	0.18	-0.17	-0.16	-0.18
Niño 3_Nov	0.32**	0.23	0.19	-0.17	-0.18	-0.18
Niño 3_Dec	0.35**	0.25*	0.21	-0.16	-0.18	-0.18
Niño 3_Jan	0.35**	0.25*	0.16	-0.20	-0.19	-0.16
Niño 3_Feb	0.36**	0.27*	0.16	-0.20	-0.19	-0.15
Niño 3_Mar	0.29*	0.31**	0.20	-0.21	-0.23	-0.19

Note: Colors and asterisks denote statistical significance: red with *** for the 99 % confidence level, green with ** for 95 %, and magenta with * for 90 %.

Among the three indices, the Niño 4 index has the largest correlation with Antarctic stratospheric circulations (Table 1). In particular, the Niño 4 index exhibits a significantly positive correlation with the subsequent July–September mean $T_{10\text{-}30}$ index, with correlations from September to March reaching the 95 % confidence level. Here, the largest correlation occurs during boreal winter (December–February), with correlation coefficients exceeding 0.30 at the 95 % confidence level ($R > 0.30$, $p < 0.05$). The January Niño 4 index shows the highest correlation with August $T_{10\text{-}30}$ ($R > 0.43$, $p < 0.01$). Additionally, the December–February Niño 4 index is significantly negatively correlated with the July–September $U_{10\text{-}30}$ index, with the largest negative correlation found between the January Niño 4 and August $U_{10\text{-}30}$ ($R = -0.40$, $p < 0.01$). These correlations are consistent with stratospheric warming (cooling) and a weakened (strong) Stratospheric polar vortex (SPV) associated with warm (cold) central Pacific SSTs.

In comparison with Niño 4, the Niño 3.4 index has weaker correlations with stratospheric temperature and zonal wind. The January Niño 3.4 has the highest correlation with July $T_{10\text{-}30}$ ($R \approx 0.38$, $p < 0.01$), while the correlation with September $T_{10\text{-}30}$ is not statistically significant. Similarly, its correlation with $U_{10\text{-}30}$ is weak, with only a marginally significant negative correlation between the January–March Niño 3.4 index and July–August $U_{10\text{-}30}$ at the 90 % confidence level. However, the Niño 3 index exhibits the weakest correlation with the polar stratosphere. While a moderate correlation with $T_{10\text{-}30}$ is observed during July–August, correlations in September are very weak and do not exceed the 90 % significance threshold.

We next examine the connection of ENSO phases in the preceding boreal winter with the Antarctic stratospheric circulation anomalies in July-September for 45 years 1980-2024 (Table 2). Here, we define a warm (cold) stratospheric year as the year when the July–September mean $T_{10\text{–}30}$ index is ≥ 0.5 (≤ -0.5) standard deviations or when the $U_{10\text{–}30}$ index is ≤ -0.5 (≥ 0.5) standard deviations. During the study period of 45 years, 14 are boreal winter El Niño years, of which 8 are followed by stratospheric warming events and 4 by cooling events, corresponding to an occurrence rate of 57 % and 28.5 %, respectively. Notably, 6 out of these 8 warming cases occur after central Pacific El Niño events. The remaining two cases, 2015/16 and 2023/24, are classified as eastern Pacific El Niño events, but are also accompanied by warm SSTs in the tropical central Pacific. By comparison, among 17 boreal winter La Niña years, 11 are followed by stratospheric cooling events and 4 by warming events, corresponding to occurrence rates of 65 % and 23.5 %, respectively. Of the 13 ENSO–neutral years, four are associated with stratospheric warming events and another four with cooling events, indicating no clear preference for either condition during neutral years.

Table 2. Relationship between ENSO phases in the preceding boreal winter and Antarctic stratospheric temperature (AST) anomalies during July–September for the 45-year period (1980–2024).

Year (DJF)	Event Type	AST Anomalies
1980–1981	Neutral	Cold (C)
1981–1982	Neutral	C
1982–1983	El Niño (EP)	C
1983–1984	La Niña	Warm(W)
1984–1985	La Niña	Normal (N)
1985–1986	Neutral	W
1986–1987	El Niño (CP)	C
1987–1988	El Niño (CP)	W
1988–1989	La Niña	C
1989–1990	Neutral	N
1990–1991	Neutral	C
1991–1992	El Niño (CP)	W
1992–1993	Neutral	N
1993–1994	Neutral	N
1994–1995	El Niño (CP)	N
1995–1996	La Niña	W
1996–1997	Neutral	W
1997–1998	El Niño (EP)	C
1998–1999	La Niña	C
1999–2000	La Niña	C
2000–2001	La Niña	C
2001–2002	Neutral	W
2002–2003	El Niño (CP)	C
2003–2004	Neutral	W
2004–2005	El Niño (CP)	W
2005–2006	La Niña	C
2006–2007	El Niño (CP)	W
2007–2008	La Niña	C
2008–2009	La Niña	C
2009–2010	El Niño (CP)	W
2010–2011	La Niña	C
2011–2012	La Niña	W
2012–2013	Neutral	N
2013–2014	Neutral	N
2014–2015	El Niño (CP)	C
2015–2016	El Niño (EP)	W
2016–2017	La Niña	W
2017–2018	La Niña	C
2018–2019	El Niño (CP)	W
2019–2020	Neutral	C
2020–2021	La Niña	C
2021–2022	La Niña	C
2022–2023	La Niña	N
2023–2024	El Niño (EP)	W

El Niño	La Niña	Neutral
Total: 14	Total: 17	Total: 13
Warm (CP) / Cold	Warm / Cold	Warm / Cold
8 (6) / 4	4 / 11	4 /4
57% / 28.5%	23.5% / 65%	31% /31%

Correlation coefficients between the July–September mean $T_{10\text{-}30}$ index and the global SST field from the preceding boreal winter are shown in Figure 1a. The highest correlation coefficients are observed in the central Pacific, particularly over the Niño 4 region. Additionally, significant positive correlations appear over the North Indian Ocean and the South Pacific, likely reflecting remote responses to ENSO (Alexander et al., 2002).

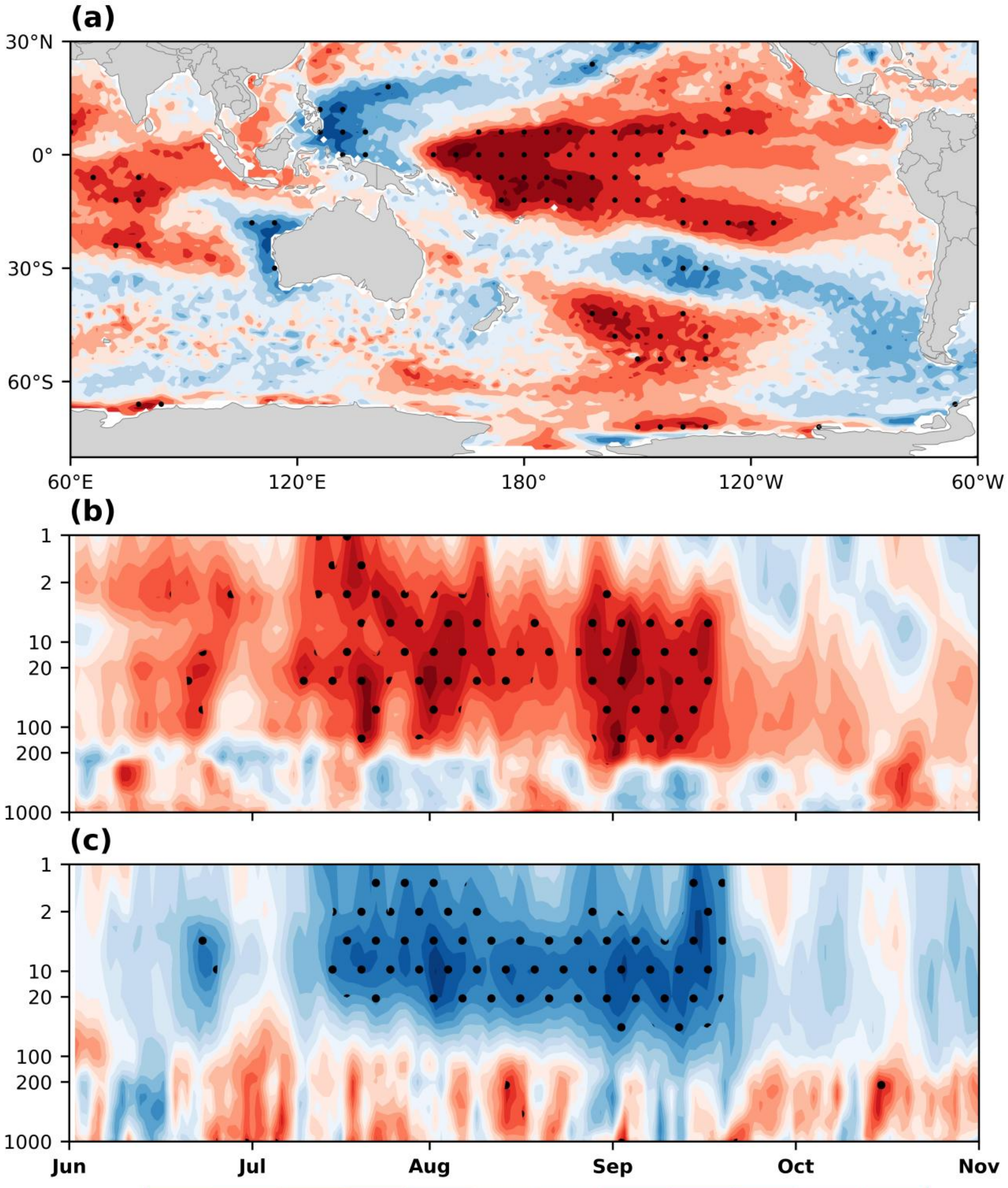

Figure 1. (a) Correlation coefficients between July–September mean $T_{10\text{-}30}$ index and January–March mean SST, (b) Correlation coefficients between December–February mean Niño 4 index and daily Temperature averaged over 60 °S–90 °S, and (c) same as (b), but for zonal-mean zonal wind averaged over 40 °S–50 °S. Black dots represent the 95 % confidence level.

The most pronounced impacts of SSTs over the Niño 4 region occur, however, above 100 hPa during the austral winter of the following year. Figs. 1b-c present the correlations between the boreal winter Niño 4 index and the Antarctic daily zonal-mean temperature (averaged over

60 °S–90 °S) and zonal-mean zonal wind (averaged over 40 °S–50 °S) from June to September of the following year. The Niño 4 index exhibits significant positive correlations with stratospheric temperature and negative correlations with zonal wind during July–September, consistent with the stratospheric warming and weakened SPV.

To further examine the impacts of Niño 4 SST anomalies on the stratospheric temperatures and the SPV, 17 warm years and 14 cold years according to ±0.5 standard of the Niño 4 index are selected to calculate composite differences in vertical zonal-mean temperature and zonal wind (Figs. 2). The ±0.5 standard deviation threshold is chosen to capture relatively strong warm and cold events, but the results are not sensitive to the specific threshold value. In June, warming is primarily observed in the upper polar stratosphere and the tropical troposphere, with the strongest signal at 1–5 hPa (Fig. 2a). As the season progresses, the warming intensifies and gradually propagates downward and poleward, with peak anomalies centered around ~50 °S in July–August (Figs. 2b–c). This warming reaches its maximum at 10 hPa around 70–90 °S in September (Figs. 2d).

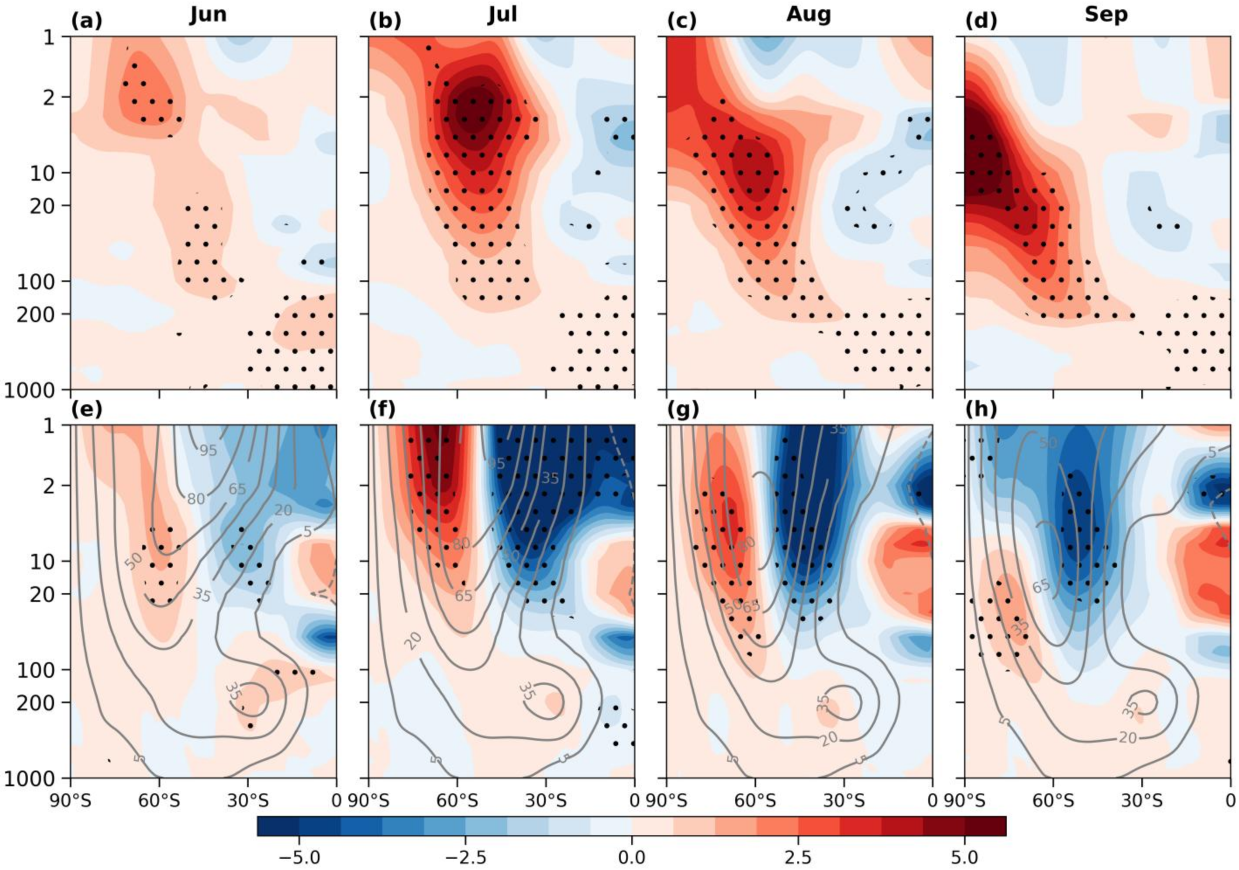

Figure 2. Composite differences between warm and cold Niño 4 years for (a,e) June, (b,f) July, (c,g) August, and (d,h) September. (a–d) Zonal–mean temperature (shaded, unit: K), and (e–h) zonal–mean zonal winds (shaded, unit: m/s), where the climatological mean of zonal-mean zonal wind is computed from 1991-2020 (contour, unit: m/s). Black dots indicate regions statistically significant at the 95% confidence level.

In general, the stratospheric warming anomalies are accompanied by a significant weakening of the stratospheric westerlies. Under climatological conditions, the polar night jet typically establishes and strengthens gradually from June to July, centered near 1 hPa and around 45 °S (Figs. 2e–f). The jet core then migrates poleward and downward in August and weakens in September (Figs. 2g–2h). However, during warm Niño 4 years, anomalous easterlies emerge south of 45 °S and anomalous westerlies develop south of 60 °S as early as June (Figs. 2e), while anomalous easterlies progressively shift poleward from July to September, substantially weakening the climatological westerlies (Figs. 2f–h), indicating a notable poleward contraction and shift of the SPV (Figs. 2f–h). This pattern reflects a delayed yet robust stratospheric response to warm SST anomalies in the tropical central Pacific.

Moreover, the atmospheric responses exhibit the maximum stratospheric warming appears over the Indian Ocean during June–September, while no significant warming is observed in the South Pacific (Fig. 3a-d). This warming pattern tends to weaken midlatitude baroclinicity, producing a westerly anomaly at high latitudes and a negative anomaly in the midlatitude in stratosphere, indicative of a contraction of the jet stream (Figs. 3e-h). Meanwhile, the stratospheric geopotential heigh show a zonal wavenumber-1 pattern, with a positive center over the Indian Ocean and a negative center over the Pacific and Atlantic, suggesting a role of planetary wave (Figs. 3i-l). The responses intensify from June to September and gradually propagate eastward and poleward (Fig. 3). For example, the maximum westerly anomalies extend into the Pacific polar region by September, while pronounced negative wind anomalies develop over the midlatitude Pacific (Fig. 3h).

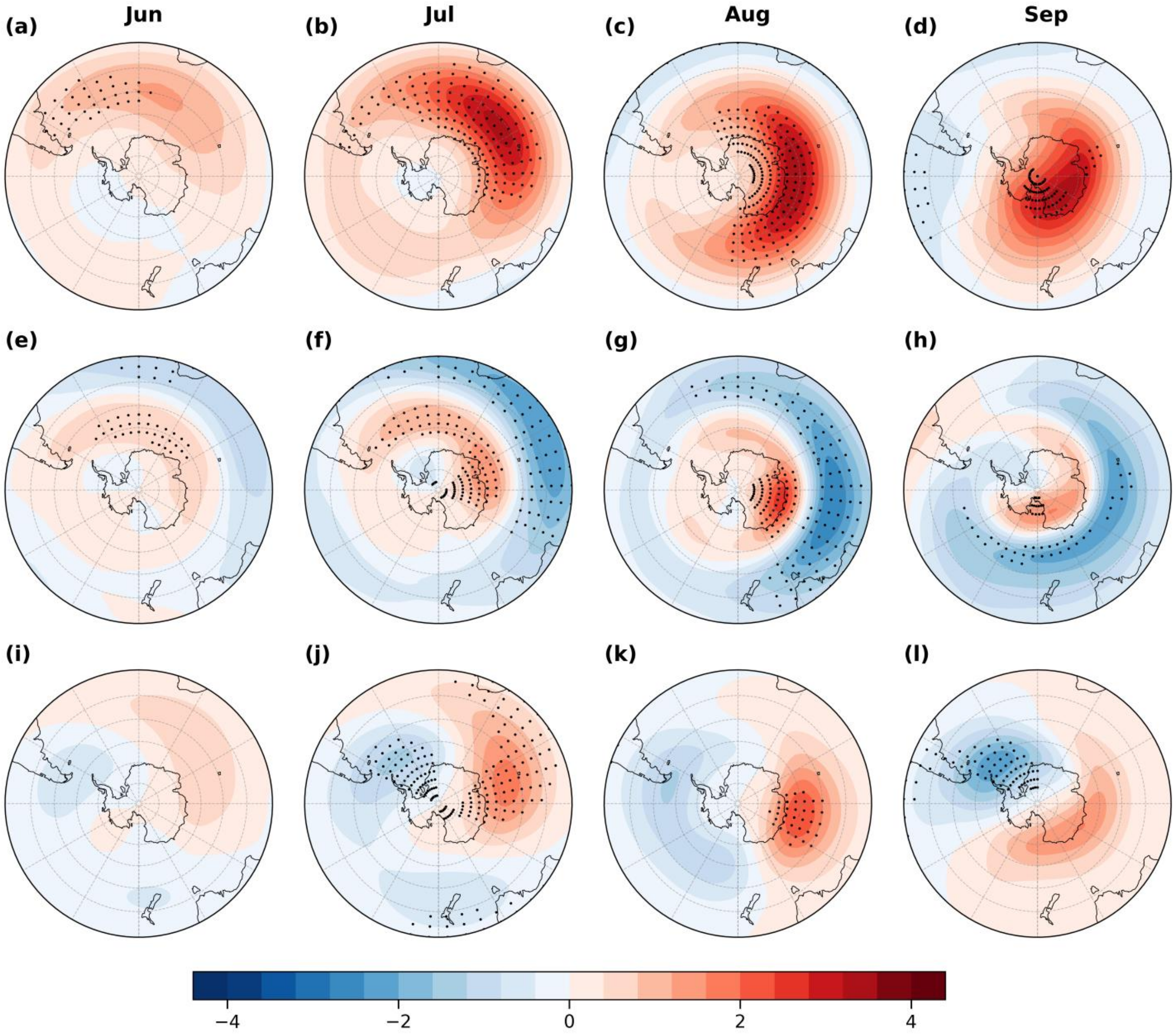

Figure 3. Composite differences between warm and cold Niño 4 years for (a,e,i) June, (b,f,j) July, (c,g,k) August, and (d,h,l) September. (a–d) Temperature averaged over 10-30 hPa (shaded, unit: 2 K), (e–h) zonal wind averaged over 10-30 hPa (shaded, unit: 5 m/s), and (i–l) geopotential height averaged over 10-30 hPa (shaded, unit: 10 dagpm). Black dots indicate regions statistically significant at the 95% confidence level.

Figures 4a–b present time series of the boreal winter Niño 4 index alongside the July–September mean $T_{10\text{-}30}$ and $U_{10\text{-}30}$ indices from 1981–2024. The Niño 4 index exhibits a significant positive correlation with the $T_{10\text{-}30}$ index ($R = 0.43$, $p < 0.01$) (Fig. 4a) and a significant negative correlation with the $U_{10\text{-}30}$ index ($R = -0.38$, $p < 0.01$) (Fig. 4b), both are significant at the 99 % confidence level, indicating that a high (low) Niño 4 index is typically associated with a warmer (colder) polar stratosphere and contracted (expanded) SPV. Notably, several prominent sudden stratospheric warming (SSW) events (e.g., 1988, 2019, 2024) coincide with positive Niño 4 SSTs (Fig. 4a). The associated stratospheric changes also influence Antarctic ozone concentrations (Wang et al., 2025). For instance, TCO_3 shows a strong positive correlation with both the T_{10-30} index ($R = 0.56$, $p < 0.01$) and the boreal winter Niño 4 index ($R = 0.36$, $p < 0.01$), both statistically significant at the 99 % confidence level (Fig. 4c). This suggests that warm (cold) Niño 4 events enhance (suppress) poleward ozone transport, thereby increasing (decreasing) ozone concentrations over Antarctica.

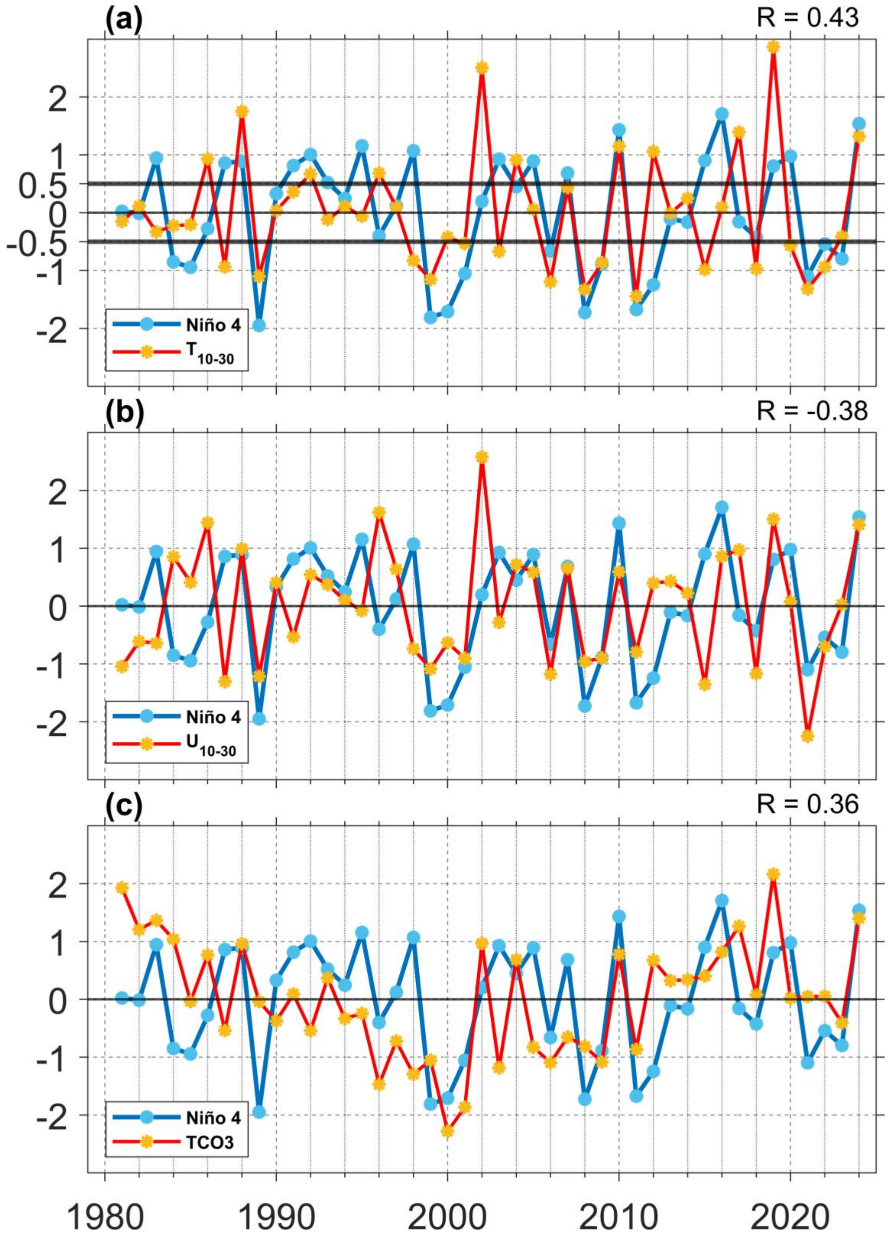

Figure 4. Time series of standardized Niño 4 index (blue line), along with (a) July–September mean T_{10-30} index (red line), (b) July–September mean U_{10-30} index (red line, multiplied by -1), and (c) July–September mean TCO_3 index (red line) from 1981 to 2024. R in the upper right corner denotes the correlation coefficient between the Niño 4 index and the T_{10-30}, U_{10-30}, and TCO_3 indices, respectively.

4 Effects of anomalous planetary waves

4.1 Stratospheric temperature and zonal wind

Previous studies suggested that polar stratospheric warming is primarily driven by the upward propagation of planetary waves from the troposphere, which disturb the SPV through wave–mean flow interactions (Baldwin et al., 2021). To evaluate the effect of planetary wave activity on Antarctic stratospheric temperature anomalies during different Niño 4 SST events, the composite differences of key atmospheric variables were calculated between warm and cold Niño 4 years, averaged over consecutive three–month periods from January to September of the following year.

During the mature phase of El Niño (January–March), positive SST anomalies develop in the central and eastern Pacific (Fig. 5a). As SST increases, convection intensifies in the central Pacific (Fig. 5d), accompanied by a negative SLP anomaly and a positive geopotential height anomaly at 250 hPa over the tropical central Pacific, indicating a barotropic response (Figs. 5g,j). Furthermore, the convection anomaly triggers a southward–propagating teleconnection wave train at 250hPa, as suggested by the TN01 flux (Vector, Fig. 5j). This wave train, known as the PSA teleconnection (Mo and Higgins, 1998), features a positive geopotential height anomaly over the southeastern Pacific (near 110 °W, 60 °S) and a negative anomaly over the southwestern Pacific (near 150 °W, 40 °S) (Fig. 5j). The warm Niño 4 SSTs and their associated convection responses over the tropical central Pacific persist into April–June (Figs. 5b,e,h,k). Although the amplitude of the high and low-pressure centers over the southeastern and southwestern Pacific weakens, the PSA wave train remains active (Fig. 5k). By July–September (austral winter), the warm Niño 4 SSTs and their associated barotropic responses begin to dissipate (Figs. 5c,i,l). However, despite the weakening of tropical convention (Fig. 5f), it is strong enough to sustain a weak mid-latitude PSA wave train, maintaining a persistent positive geopotential height anomaly over the southeastern Pacific and a negative anomaly over the South Atlantic, as indicated by the TN01 flux (Fig. 5l).

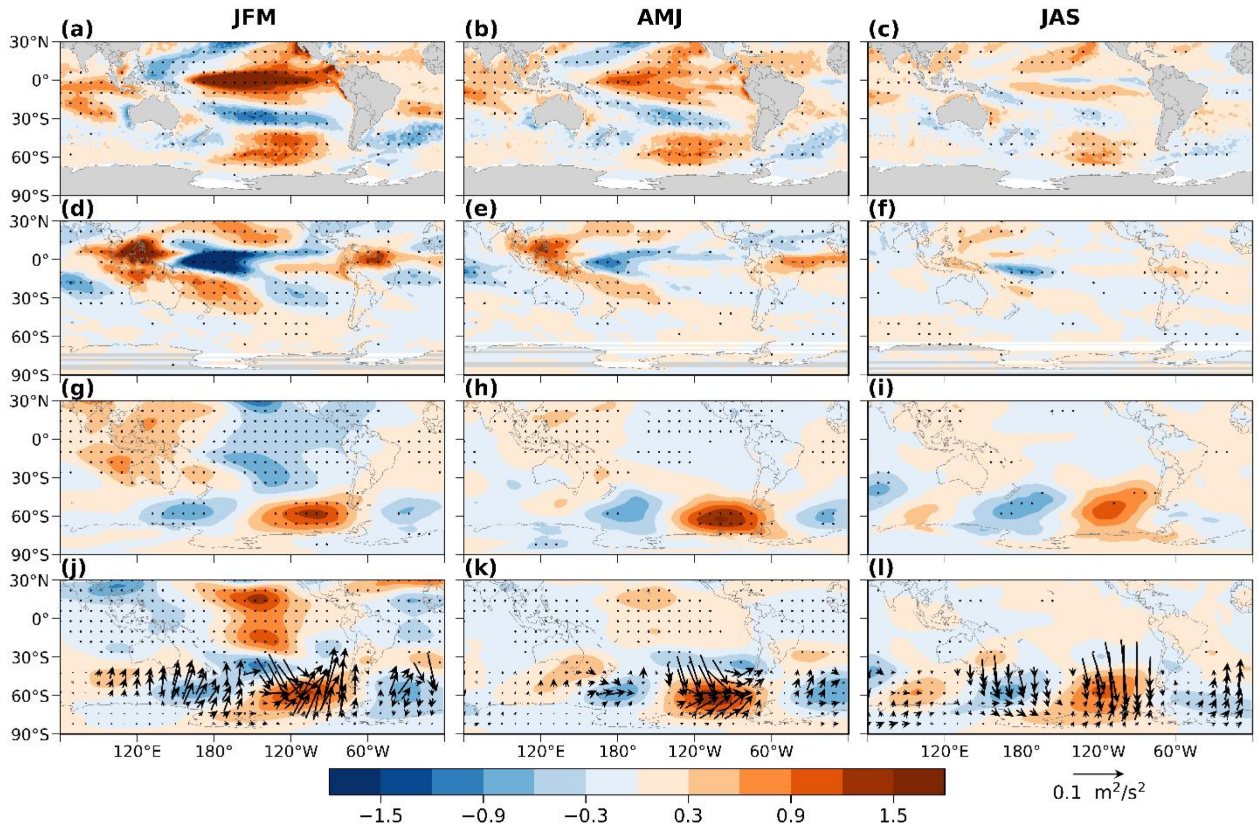

Figure 5. Composite differences between warm and cold Niño 4 years. The panels show three–month means for January–March (left column), April–June (middle column), and July–September (right column). (a–c) Sea surface temperature (SST, shaded, unit: K), (d–f) outgoing longwave radiation (OLR, shaded, unit: $1.5\times10e^6$ w/m^2), (g–i) sea level pressure (SLP, shaded, unit: 300 Pa), (j–l) Geopotential heights (shaded, unit: 5 dagpm) and TN01 flux (vector, unit: 0.1 m^2/s^2) at 250 hPa. Black dots indicate regions statistically significant at the 95% confidence level.

The geopotential height anomaly extends into the lower stratosphere and remains statistically significant at 100 hPa (Fig. 6). The climatological geopotential height at 100 hPa is characterized by a wave-1 pattern, featuring a positive center over the South Pacific and a negative center over the Atlantic Ocean and Indian Ocean sectors (contour lines in Fig. 6). During January-February-March (JFM) (austral summer), geopotential height anomalies associated with warm central Pacific SSTs form a wave train, with a positive center over the southeastern Pacific and two negative centers over the southwestern Pacific and the southern Atlantic (Fig. 6a). However, this pattern does not align well with the climatological wave-1 structure, indicating a displacement of the wave pattern (Fig. 6d). Moreover, the anomalous wave-1 centers at high latitudes are not statistically significant (Fig. 6d). Although the wave-1 component of the geopotential height shows a westward tilt with altitude and broadly resembles with the climatological structure, this alignment is only statistically significant below 500 hPa (Fig. 6g). As a result, planetary waves are not substantially amplified in the lower stratosphere, primarily due to the prevailing easterly winds in the upper stratosphere over Antarctica in JFM (contours, Fig. 7a), which inhibit upward propagation of planetary waves (Baldwin et al., 2021). This is further supported by the E–P flux vectors, which show that planetary wave propagation is largely confined below 50 hPa in the mid– and low–latitudes (Fig. 7a).

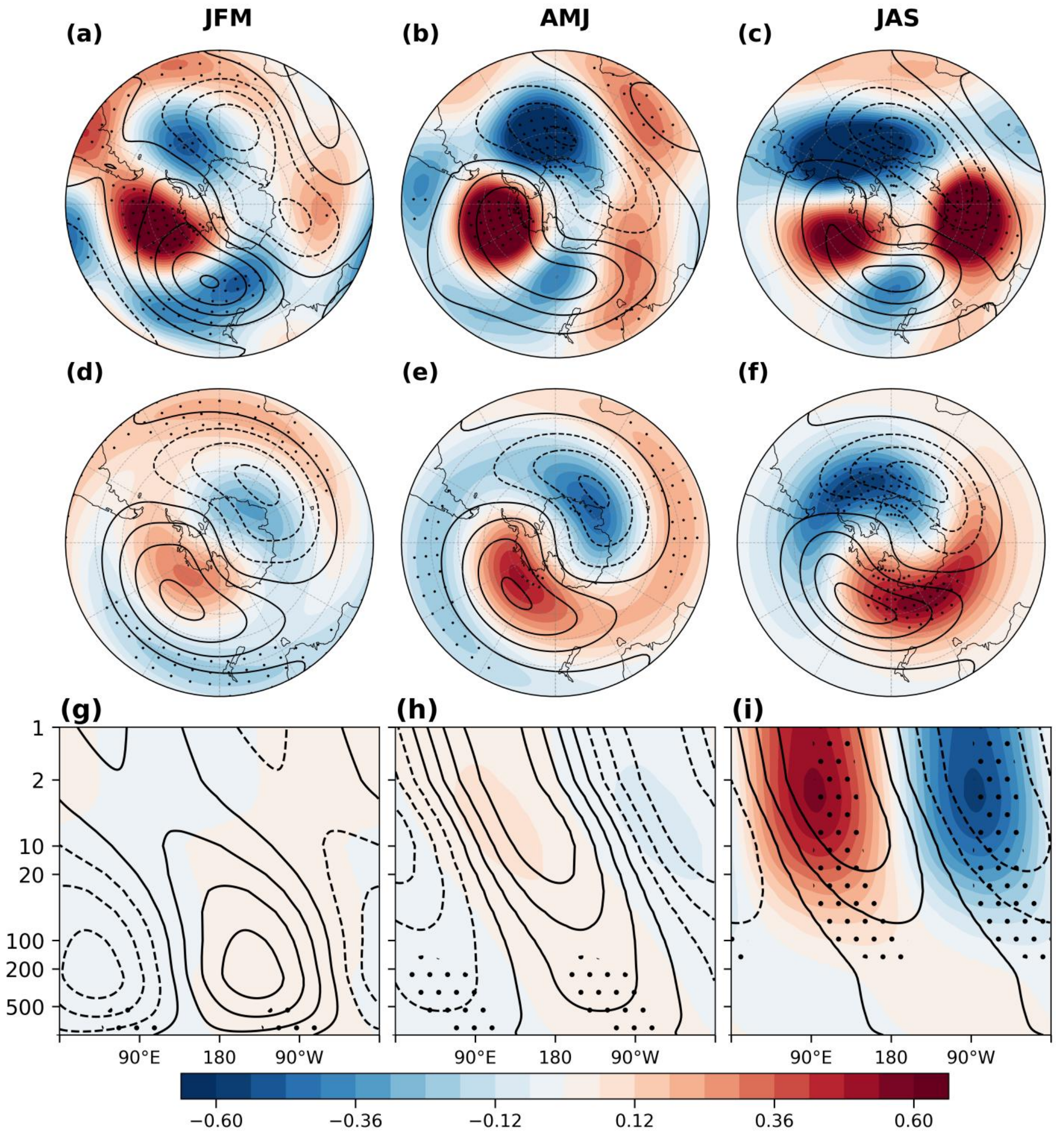

Figure 6. Composite differences between warm and cold Niño 4 years. The panels show three–month means for January–March (left column), April–June (middle column), and July–September (right column). (a–c) Geopotential heights at 100 hPa (shaded, unit: 5 dagpm), (d–f) wave-1 of geopotential heights at 100 hPa (shaded, unit: 5 dagpm), and (g–i) wave-1 of geopotential heights averaged over 45 °S–75 °S at 1000–1hPa (shaded, unit: 30 dagpm). The climatological geopotential height is calculated from 1991–2020 (contours, unit: dagpm). Black dots indicate regions statistically significant at the 95% confidence level.

During April-May-June (AMJ), the positive geopotential height center over the southeastern Pacific and the negative center over the southern Atlantic become more pronounced (Fig. 6b), aligning more closely with the climatological wave-1 pattern (Fig. 6e). This alignment contributes to a westward tilt of the geopotential height field with altitude (Fig. 6h). However, this vertical tilt is only statistically significant below 100 hPa (Fig. 6h). During this period, stratospheric zonal winds gradually transition to a westerly regime, but large portions of the upper polar stratosphere continue to experience weak westerlies or even easterlies (contours, Fig. 7b). As a result, a significant portion of the planetary waves are refracted equatorward, and their ability to disturb the polar stratosphere remains limited (Fig. 7b).

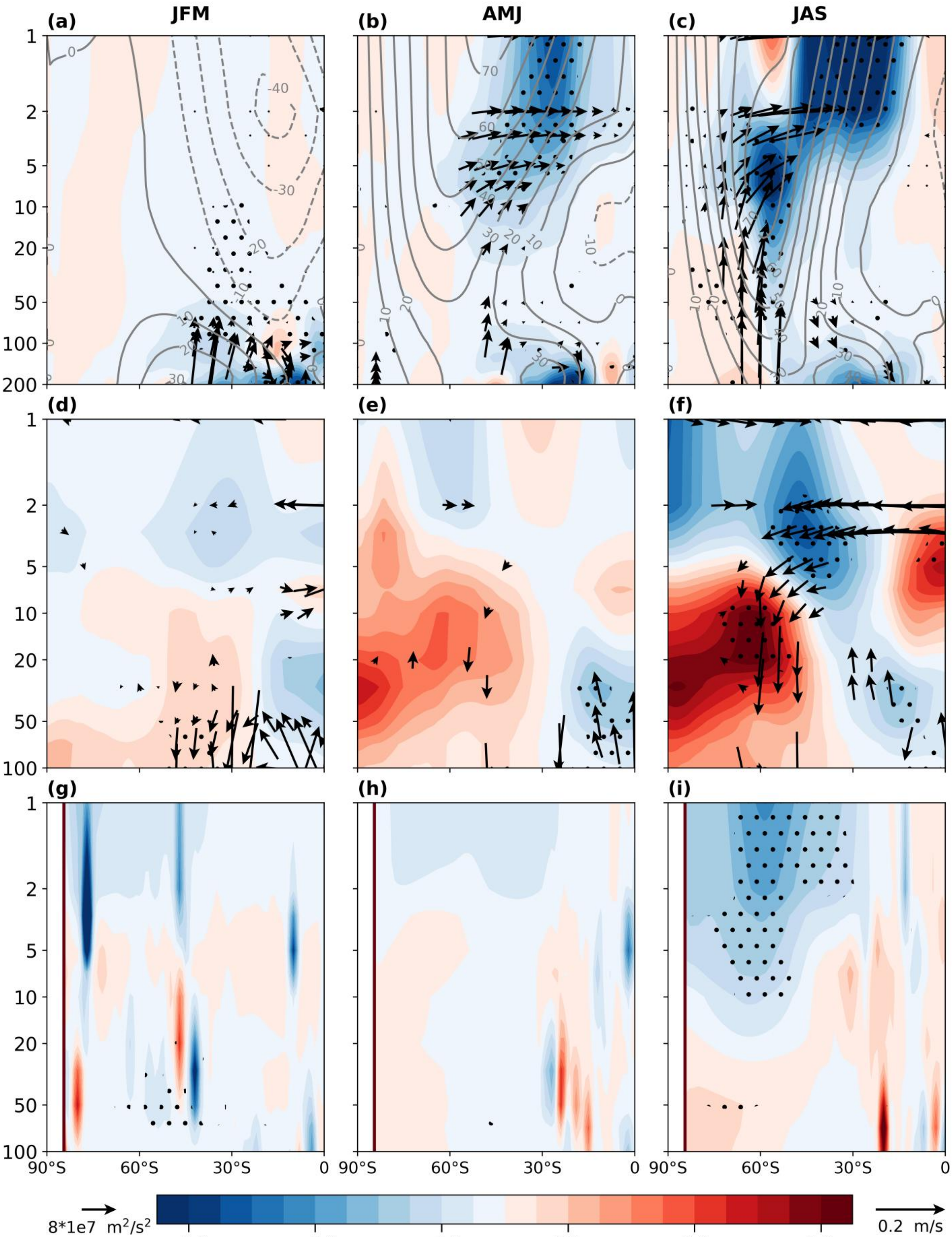

Figure 7. Composite differences between warm and cold Niño 4 years. The panels show three–month means for January–March (left column), April–June (middle column), and July–September (right column). (a–c) E-P flux (vector: m^2/s^2) and its divergence (shaded, unit: 60 m/s/day), where the climatological zonal-mean zonal wind are calculated from 1991–2020 (contours, unit: m/s), (d–f) ozone mass mixing ratio (shaded, unit: $3\times1e^{-6}$ kg/kg) and residual mean circulation (vector, unit: m/s), and (g–i) wave reflective index (shaded, unit: %). Black dots indicate regions statistically significant at the 95% confidence level.

During July-August-September (JAS), the geopotential height centers over the southeastern Pacific weaken, while the positive center over the southern Indian Ocean strengthens significantly (Fig. 6c). This spatial pattern enhances the climatological wave-1 trough and ridge structure (Fig. 6f) and exhibits a westward tilt of the geopotential height field with altitude, which becomes statistically significant in the stratosphere (Fig. 6i). Although the wave-2 pattern exhibits a strong amplitude, it is nearly orthogonal to the climatological wave-2 phase during July–September. Therefore, the wave-2 component is not reinforced, and the process is mainly dominated by the wave-1 pattern (Figures not shown). During this period, the polar regions enter the polar night, with minimal solar heating, which increases baroclinicity in the mid– and high–latitudes. The stratosphere becomes fully dominated by strong westerly winds, creating favorable conditions for the upward propagation of planetary waves into the polar stratosphere (contour lines, Fig. 7c). In addition, the wave reflection index exhibits a significant negative anomaly south of 30 °S in the upper stratosphere (Fig. 7i). This further indicates that planetary waves are strongly refracted toward the mid- and high-latitude stratosphere (Fig. 7c). Based on the E–P flux theorem (Matusno, 1971), when E-P flux convergence occurs in the midlatitudes, the jet stream tends to weaken and poleward heat transport increases. During July–September, the strong Antarctic polar vortex inhibits the poleward propagation of planetary waves, resulting in relatively weak polar warming and stronger warming in the subpolar and midlatitude regions. As a result, significant high-latitude warming and contraction of the polar vortex are observed during April-September (Fig 3).

This relationship is reversed under cold Niño 4 SST conditions. Specifically, when cold SST anomalies occur in the central tropical Pacific, planetary wave activity and their associated disturbances to the stratosphere are suppressed, leading to polar stratospheric cooling and a strengthening SPV.

4.2 Mid-latitude sea-air interactions

4.2.1 Ocean responses

Niño 4 SSTs influence mid-latitude ocean temperatures through atmospheric teleconnections. During JFM, a positive Niño 4 SSTs trigger a PSA teleconnection pattern, resulting in a high-pressure anomaly centered near 110 °W, 60 °S over the southeastern Pacific (Figs. 5j and

7g). The associated poleward surface winds and adiabatic subsidence warm the lower troposphere (Figs. 8a,d), while the ocean gains heat, as indicated by the negative net heat flux anomaly, defined as the sum of latent and sensible heat fluxes, long-wave radiant and short-wave radiant heating (Fig. 8m), leading to a localized SST warming (Fig. 8g). Simultaneously, there is a modest reduction in SIC in the Amundsen and Ross Seas (Fig. 8j).

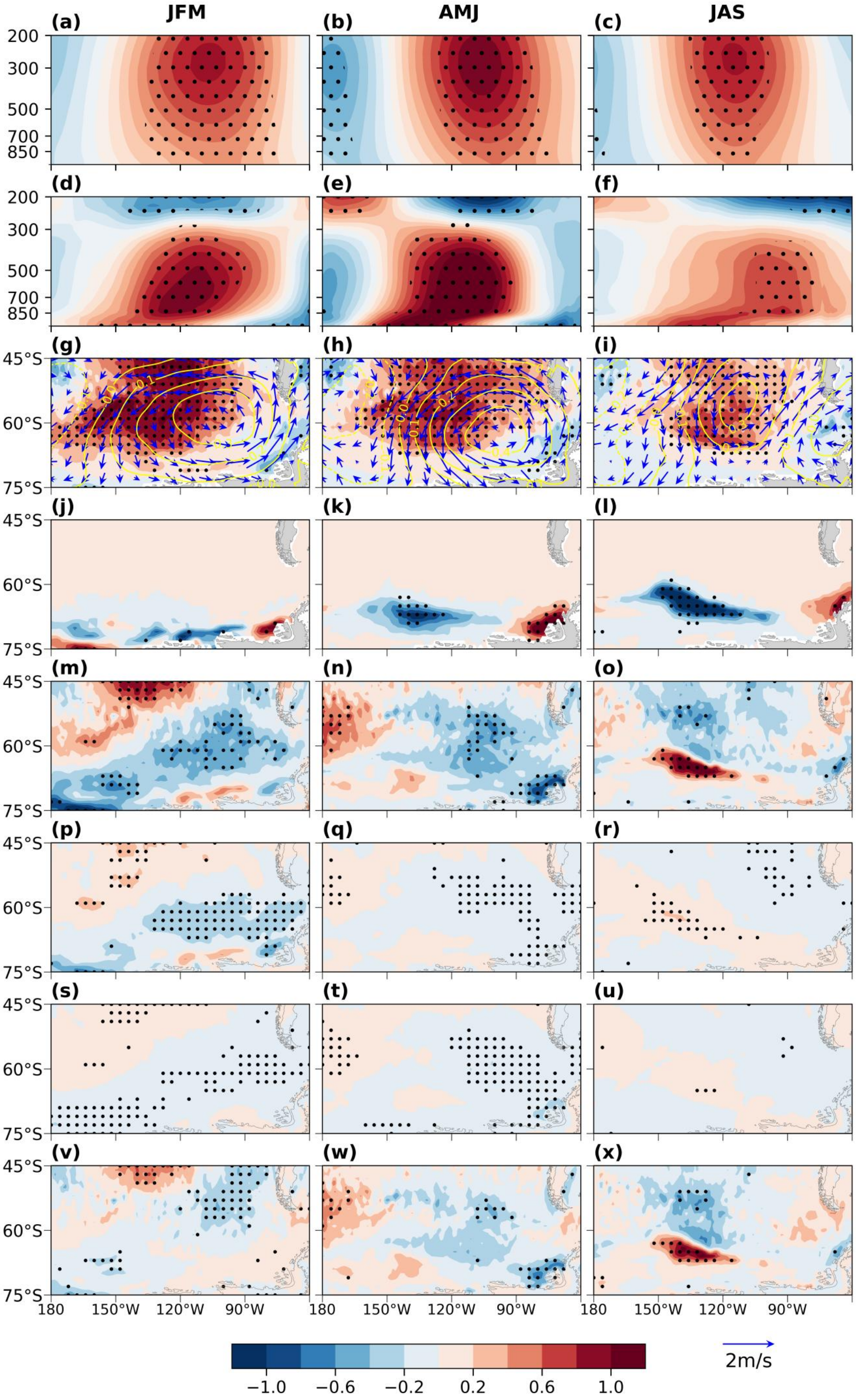

Figure 8. Composite differences between warm and cold Niño 4 years. The panels show three–month means

for January–March (left column), April–June (middle column), and July–September (right column). (a–c) Geopotential heights (shaded, unit: 5 dagpm), averaged over 45 °S–75 °S, (d–f) temperatures (shaded, unit: K), averaged over 45 °S–75 °S, (g–i) SST (shaded, unit: K), SLP (contours, unit: 1000 Pa), and 10-meter winds (vector, unit: 2 m/s), (j–l) sea ice concentration (SIC, unit: 100 %), (m-o) net upward total heat flux (the sum of turbulence heat flux, upward long-wave heat flux and net downward short-wave radiation, shaded, unit: 3 W/m^2), (p-r) net downward short-wave radiation (shaded, unit: 3 W/m^2), (s-u) upward long-wave radiation (shaded, unit: 3 W/m^2), and (v-x) turbulence heat flux (the sum of latent and sensible heat flux; shaded, unit: 3 W/m^2). Black dots indicate regions statistically significant at the 95% confidence level.

A similar pattern persists during AMJ (Figs. 8b,e). The PSA pattern associated with warm Niño 4 SSTs remains evident (Fig. 5k), although the area of negative net heat flux contracts (Fig. 8n), and continues to support elevated SSTs in the southeastern Pacific through ongoing sea-air heat exchange (Fig. 8h). As a result, SIC in the Amundsen and the Ross Seas declines further (Fig. 8k). Additionally, sustained tropospheric warming enhances geopotential height anomalies in both the troposphere and lower stratosphere (Figs. 8b,e).

4.2.2 Ocean feedback to the atmosphere

While the tropospheric warming center is located between 500 hPa and 850 hPa during JFM and AMJ, the maximum warming shifts below 850 hPa in JAS, suggesting an increased influence from the ocean surface (Figs. 8d-f). During the JAS, the Niño 4 SST warming weakens (Fig. 5c), indicating a reduced influence of equatorial central-Pacific SSTs. Nevertheless, due to the ocean's large heat capacity, warm SSTs in the southeastern Pacific persist (Fig. 8i), although with reduced amplitude, implying that the accumulated heat is gradually being released (Fig. 8o). A pronounced positive geopotential height anomaly associated with the PSA pattern also remains over this region (Fig. 5l), likely sustained by local sea–air interactions.

In JAS, surface net heat flux is largely associated with sea-ice loss in the Amundsen and Ross Seas (Figs. 8l,o). Specifically, the sustained warm SSTs drive substantial sea-ice loss. Comparison between surface heat flux (Fig.8o) and ice concentration (Fig.8l) shows ice loss has a pronounced impacts on surface heat flux. During JAS, solar short-wave radiation reaches its minimum, and its contribution to the net heat flux is relatively small. (Fig. 8r). The primary contributions come from turbulence heat fluxes (Fig. 8x) and temperature advection (Fig 8i), while the contribution from longwave radiation is relatively weak (Fig. 8u). During this stage, southerly anomalies dominate the region over 40°–60°S, 90°–140°W, which transport warm air from tropical regions to the midlatitudes and enhance ocean heat uptake from atmosphere.

Although the negative net heat flux anomalies persist north of 60 °S, their intensity is relatively weak. In contrast, significant oceanic heat is released to the atmosphere in the regions where sea-ice has retreated (Fig. 8o), warming the lower troposphere (Fig. 8f) and sustaining the positive geopotential height anomaly by lifting isobaric surfaces (Fig. 8c). Notably, while net heat flux is dominated by ocean heat uptake during JFM and AMJ, the influence of sea-ice loss becomes predominant in JAS, resulting in net heat release from the ocean to the atmosphere (Figs. 8m-o). This positive feedback reinforces the Southern Hemisphere zonal-wave pattern and amplifies the planetary wave anomalies (Zi et al., 2025). Recent modeling studies also suggest that sea ice loss in the Amundsen Sea and the broader Antarctic region can have pronounced impacts on stratospheric polar vortex (Song et al., 2025). The loss of sea ice tends to sustain the influence of Niño 4 SST on stratospheric temperatures during JAS by enhancing surface heat fluxes (Fig.8).

4.3 Ozone transport

The enhanced planetary wave activity associated with the Niño 4 SST warming not only warms the polar stratosphere but also significantly alters the B–D residual circulation and polar ozone transport (Wang et al., 2025). Figures 7d–7f present the composite differences in the zonal-mean residual circulation and ozone mass mixing ratio between warm and cold Niño 4 years, each averaged over three–month periods from January to September of the following year.

During JFM, convective anomalies in the tropical Pacific Ocean drive changes in the residual circulation (Fig. 5d), resulting in decreases to the ozone mass mixing ratio in the tropical lower stratosphere and increased values in the mid–latitude lower stratosphere (Fig. 7d). However, upward–propagating planetary waves are largely confined below 50 hPa in the mid– and low–latitudes (Fig. 7a), strengthening the residual circulation primarily north of 60 °S. As a result, ozone transport to higher altitudes and into the polar region remains limited (Fig. 7d). In AMJ, although convective anomalies in the tropical Pacific Ocean persist and wave activity increases in the upper stratosphere (Fig. 7b), many of the waves are refracted equatorward, resulting in only modest polar ozone transport (Fig. 7e). In JAS, however, upward–propagating planetary waves are strongly refracted toward mid– and high–latitudes, enhancing the residual circulation and promoting both poleward and upward ozone transport (Fig. 7f). The increased poleward ozone transport enhances solar radiation absorption, playing an important role in the polar stratospheric warming through dynamical–chemical coupling (Solomon et al., 2016). In addition, adiabatic warming associated with descending air in the residual circulation further contributes to the stratospheric warming over the polar region.

5 Multivariate regression model

Nino 4 SST anomalies can influence stratospheric temperatures through the PSA pattern, which affects surface conditions at high latitudes during boreal winter. During JAS, the atmospheric circulation associated with the PSA pattern can enhance surface heat transport (Fig. 8i) and help sustain the stratospheric response (Figs. 8c, f).

The preceding analyses reveal that boreal winter Niño 4 SSTs exert a significant lagged influence on the Antarctic stratospheric circulation during the subsequent austral winter. This finding has important implications for the seasonal prediction of stratospheric variability. However, although the boreal winter Niño 4 index is significantly correlated with July–September mean $T_{10\text{-}30}$ index, it accounts for only 18.5 % of the variance in stratospheric temperature ($R^2 = 0.185$). To more interpret variability in the Antarctic stratosphere, additional factors need to be considered.

Previous studies found that the PSA teleconnection associated with Niño 4 SSTs is a key mechanism influencing the Antarctic stratosphere. The PSA pattern is represented by the second EOF mode of monthly SLP anomalies (Fig. 9). The corresponding PSA index is defined as the time series of this EOF mode. During boreal winter, the PSA index is significantly correlated with the Niño 4 index ($R = 0.40$, $p < 0.01$), suggesting that Niño 4 SSTs modulate the PSA pattern. However, the correlation between the June PSA index and the Niño 4 index is not significant ($r = 0.28$, $p > 0.05$). In addition , the June PSA index is significantly correlated with Antarctic sea ice ($r = 0.49$, $p < 0.01$), suggesting that the June PSA pattern may be maintained by sea ice anomalies and another factors. Furthermore, correlating the PSA index from December to the following September with the July–September mean $T_{10\text{-}30}$ index shows that the June PSA index exhibits the strongest correlation (Table 3, $R = 0.47$, $p < 0.01$). Interestingly, the June PSA index is only moderately correlated with the winter Niño 4 index ($R = 0.28$, $p > 0.05$), indicating that it partially captures independent variability.

Table 3. Correlation coefficients between sea ice concentration indices ($\mathrm{SIC}_{\mathrm{AR}}$) over the Amundsen and Ross Seas (averaged over 180 °W–90 °W) , sea surface temperature indices over the South Pacific ($\mathrm{SST}_{\mathrm{SP}}$) and Pacific–South America teleconnection (PSA) and July–September mean zonal-mean temperature index ($\mathrm{T}_{10\text{-}30}$) averaged over 60 °S to 90 °S.

	$\mathrm{SIC}_{\mathrm{AR}}$	$\mathrm{SST}_{\mathrm{SP}}$	PSA
Jan	-0.18	0.25	0.32^{**}
Feb	-0.08	0.27^{*}	0.21
Mar	-0.18	0.29^{*}	0.28^{*}
Apr	-0.24	0.30^{**}	-0.12
May	-0.38^{***}	0.27^{*}	0.10
Jun	-0.44^{***}	0.32^{**}	0.47^{***}
Jul	-0.23	0.30^{**}	0.03
Aug	-0.28^{*}	0.30^{**}	0.29^{*}
Sep	-0.31^{**}	0.29^{*}	0.05

Note: Colors and asterisks denote statistical significance: red with *** for the 99 % confidence level, green with ** for 95 %, and magenta with * for 90 %.

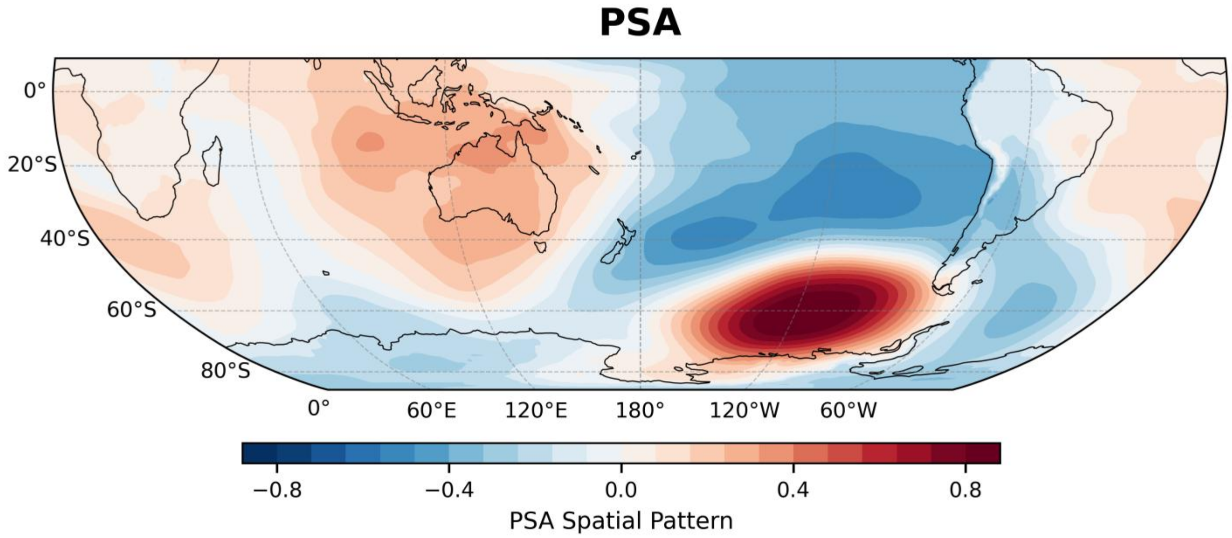

Figure 9. PSA teleconnection pattern represented by the second EOF mode of monthly SLP.

As a result, a multivariate linear regression (MLR) model is used to quantitatively assess the linear relationship between the stratospheric temperature index ($\mathrm{T}_{10\text{-}30}$) and potential factors including the Niño 4 index and PSA index. We have

$$T_{10-30} = \beta_0 + \beta_1\, Ni\tilde{n}o4 + \beta_2\, PSA + \varepsilon \qquad (7)$$

where β_0 is the intercept, β_1, β_2 are the regression coefficients associated with each factor, and ε denotes the residual error term. Prior to the regression analysis based on Eq. (7), all input time series are standardized. The regression analysis is performed using MATLAB's fitlm function, which yields estimates of regression coefficients, standard errors, t-statistics, and p-values, along with overall model diagnostics, such as the coefficient of determination (R^2) and the F-statistic. To evaluate the significance of individual factors, three confidence levels are adopted: 90 %, 95 %, and 99 %, corresponding to p-value thresholds of 0.1, 0.05, and 0.01, respectively. Factors with p-values below these thresholds are considered statistically significant. The overall performance and goodness-of-fit of the model are assessed using the R^2 metric.

To predict the July–September mean $T_{10\text{-}30}$ index, the boreal winter Niño 4 (Niño $4_{\_DJF}$) index and the June PSA ($PSA_{\_Jun}$) index are used as factors in Eq. (7). We yield

$$T_{10-30} = 0.324\, Niño4_{\_DJF} + 0.384\, PSA_{\_Jun} + \varepsilon \qquad (8)$$

with $\beta_0 = 0$. This linear regression model yields a coefficient of determination (R^2) of 0.321, indicating that the factors collectively explain approximately 32 % of the variance in the July–September mean $T_{10\text{-}30}$ index. The model's F-statistic is 9.71 with a corresponding p-value of 0.00035, which is significant at the 99 % confidence level. Among the factors, Niño $4_{\_DJF}$ and $PSA_{\_Jun}$ exhibit statistically significant regression coefficients ($p = 0.0201$ and $p = 0.0065$, respectively), confirming their primary roles in modulating stratospheric temperature.

To assess model performance, the regression–based fitted index (referred to as NP_{fit}) was compared with observed July–September mean $T_{10\text{-}30}$, $U_{10\text{-}30}$, and TCO_3 (Fig. 10). The NP_{fit} index shows significant correlation with observed values for $T_{10\text{-}30}$ ($R = 0.57$, $p < 0.01$), $U_{10\text{-}30}$ ($R = -0.55$, $p < 0.01$), and TCO_3 ($R = 0.32$, $p < 0.05$), all of which exceed the corresponding correlation values ($R = 0.4$, -0.38 and 0.36) obtained using Niño 4 index alone (Fig. 2). While the boreal winter Niño 4 index plays a key role in Antarctic stratospheric temperature variability, incorporating the June PSA index further improves the explanation of this variability. This underscores the importance of both tropical forcing and extratropical feedback processes in modulating polar stratospheric circulation.

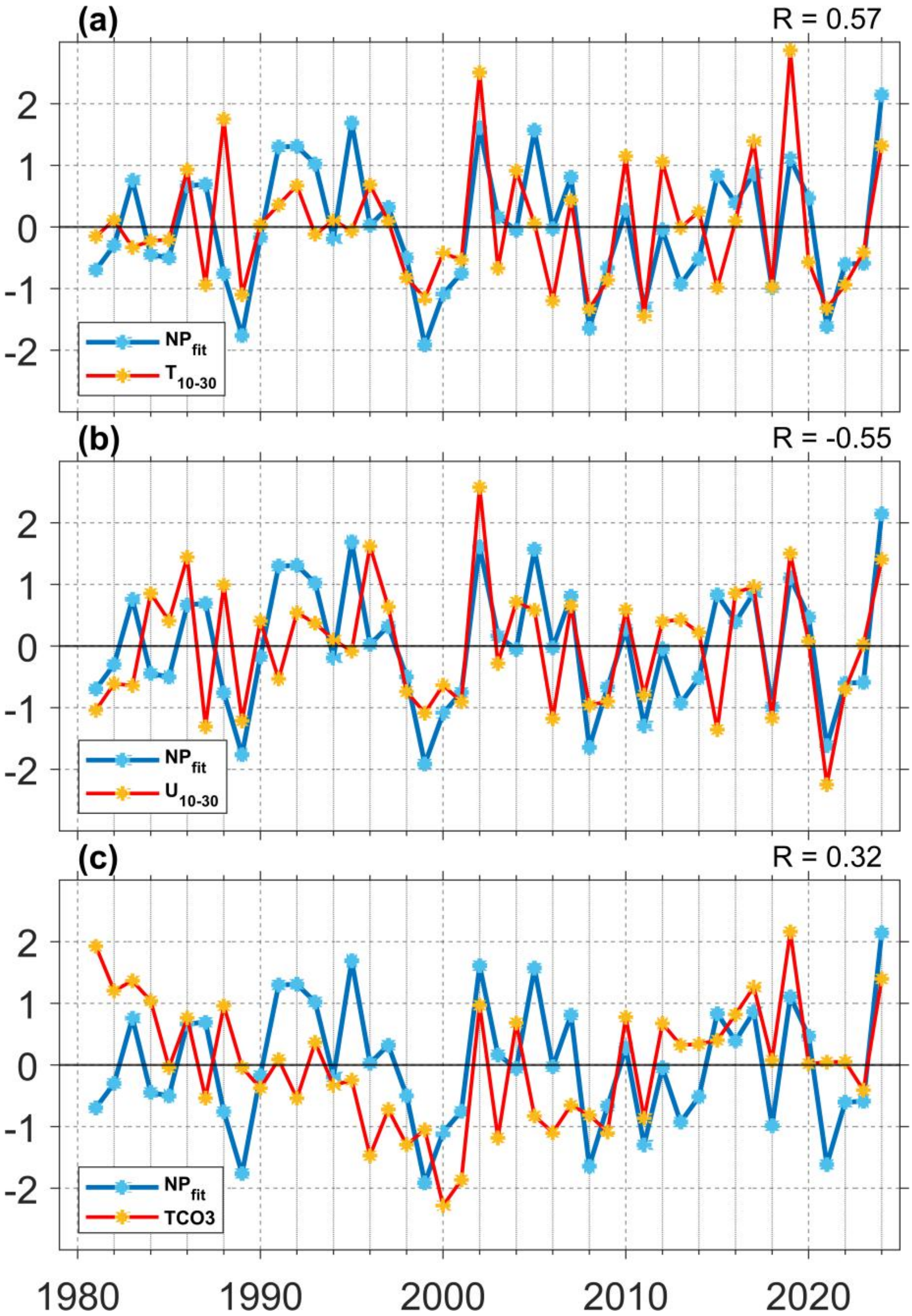

Figure 10. Time series of the standardized NP$_{fit}$ index (blue line), along with (a) July–September mean T$_{10-30}$ index (red line), (b) July–September mean U$_{10-30}$ index (red line, multiplied by -1), and (c) July–September mean TCO$_3$ index (red line) from 1981 to 2024. R in the upper right corner is the correlation coefficient between NP$_{fit}$ index and T$_{10-30}$, U$_{10-30,}$ and TCO$_3$ indices, respectively.

6 CMIP6 results

To further assess the cross-seasonal effects of tropical central Pacific SST anomalies on

Antarctic stratospheric temperatures, 20 CMIP6 historical fully-coupled model simulations for the period 1951-2014 are examined. Consistent with observations, the July–September mean polar-cap (60°–90°S) mean stratospheric temperature at 10 hPa (T_{10}) exhibits a robust positive correlation with tropical central Pacific SSTs in most CMIP6 simulations (Fig.11). Statistically significant correlations are found significant in simulations from CESM2, EC-Earth3-AerChem, EC-Earth3-Veg, EC-Earth3-CC, GISS-E2-1-G, MPI-ESM-1-2-HAM, MPI-ESM1-2-LR, E3SM-1-1-ECA, ACCESS-CM2, and CanESM5-1. Although several models (e.g., CESM2-WACCM, E3SM-1-0, HadGEM3-GC31-LL, BCC-CSM2-MR, CAS-ESM2-0, FIO-ESM-2-0, SAM0-UNICON) dot not show statistically significant results, they nevertheless display a positive correlation pattern in the tropical central Pacific. In addition, the simultaneous correlations between July-September T10 and SSTs show a statistically significant positive correlation over the southeastern Pacific (Fig. 12). Similarly, correlations with sea-ice concentration in the Amundsen Sea and Ross Sea exhibit strong negative values in most models, although a few (e.g., EC-Earth3-AerChem, EC-Earth3-Veg, CIESM, E3SM-1-1-ECA) display weaker correlations (Fig. 13).

Overall, these results are consistent with observations and support the presence of a cross-seasonal linkage between tropical central Pacific SST anomalies and Antarctic stratospheric polar temperatures.

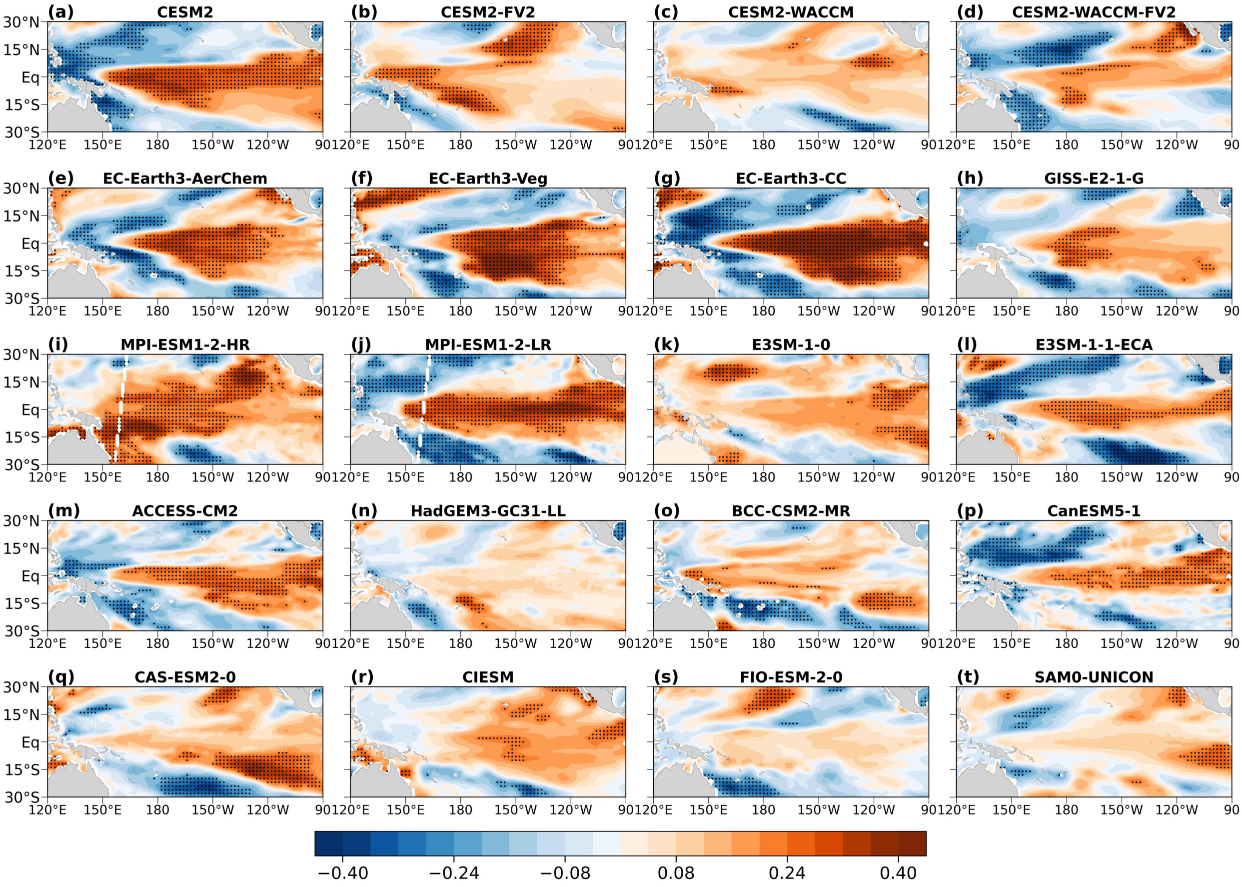

Figure 11. Correlation between January–March mean SST and July–September mean T_{10} index (shaded). Black dots indicate regions statistically significant at the 90% confidence level.

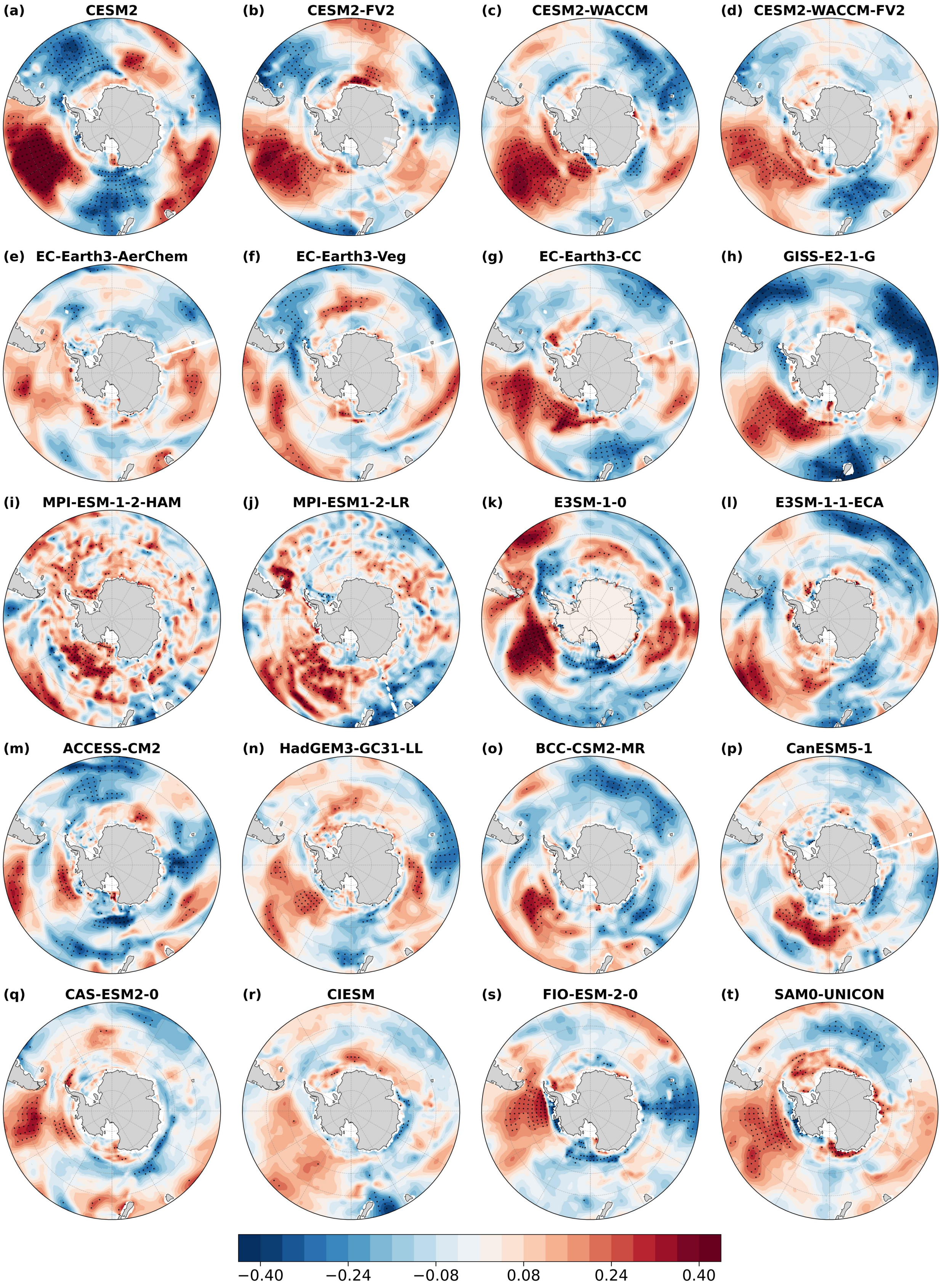

Figure 12. Correlation between July–September mean SST and July–September mean T_{10} index (shaded). Black dots indicate regions statistically significant at the 90% confidence level.

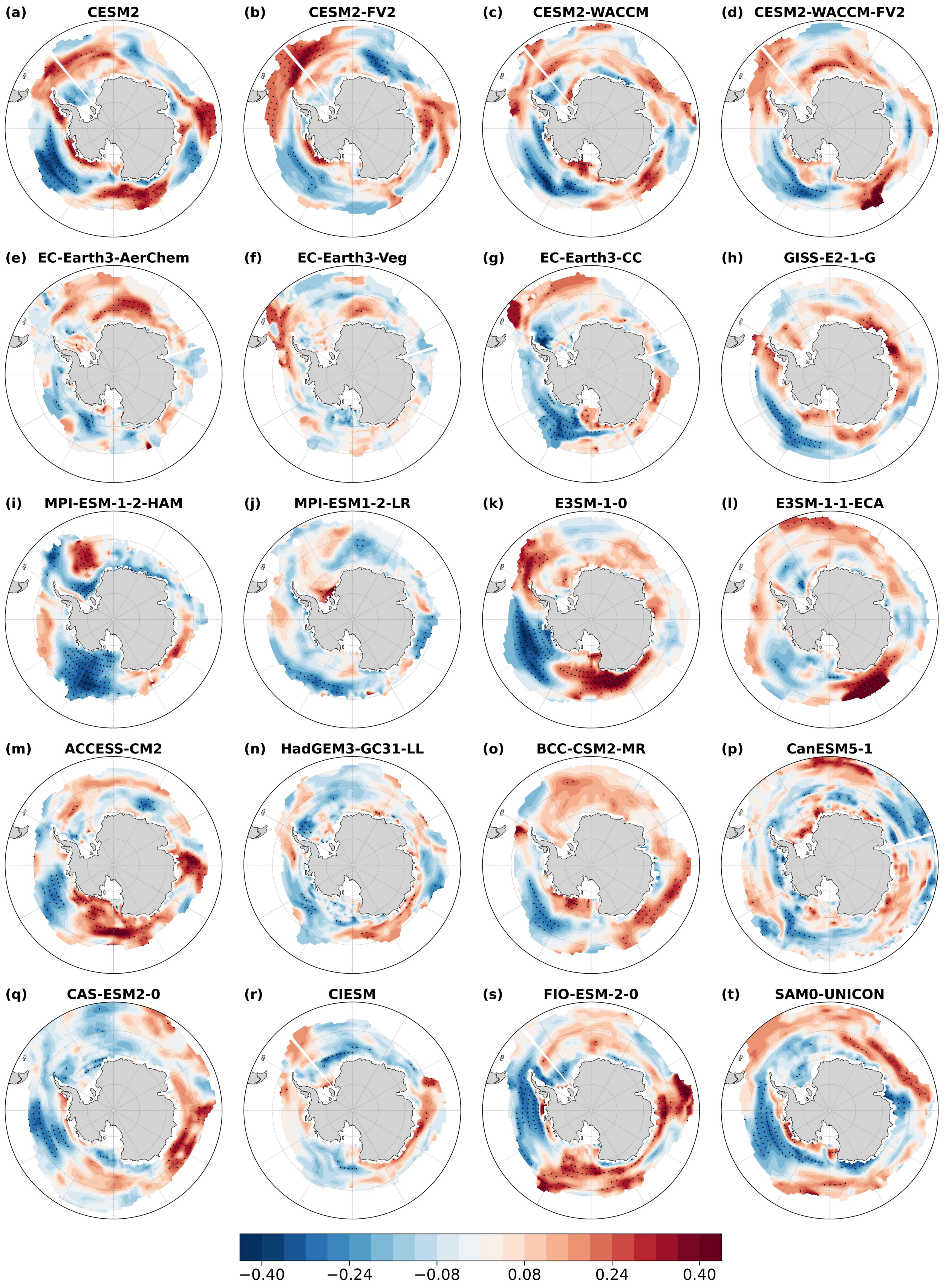

Figure 13. Correlation between July–September mean SIC and July–September mean T_{10} index (shaded). Black dots indicate regions statistically significant at the 90% confidence level.

7 Conclusions and discussions

The cross–seasonal influence of the El Niño–Southern Oscillation (ENSO) on Antarctic stratospheric circulation was investigated in this study using ERA5 reanalysis of 45 years (1980–2024). Our analysis revealed that sea surface temperature (SST) anomalies have a significant impact on the stratospheric temperatures. Specifically, warm (cold) SST anomalies (SSTs) in the Niño 4 region (Central Pacific) during boreal winter are followed by significantly warming (cooling) of the Antarctic stratosphere in the subsequent austral winter (July–September), accompanied by a weakening (strengthening) of the stratospheric polar vortex (SPV). Among the ENSO indices (Niño 3, Niño 3.4, Niño 4), the boreal winter Niño 4 index exhibits the strongest and most robust correlation with the July–September polar stratospheric temperature ($T_{10\text{-}30}$) index, reaching $R \approx 0.43$ ($p < 0.01$). In contrast, correlations with Niño 3.4 and Niño 3 indices (Eastern Pacific) are substantially weaker, suggesting that Niño 4 SSTs are the primary drivers of the observed Antarctic stratospheric responses. In addition to the observational analyses, the fully coupled simulations from 20 CMIP6 models also reproduce the cross-seasonal connection between tropical central Pacific SST anomalies and Antarctic stratospheric temperature anomalies, providing further evidence for the robustness of this teleconnection.

The underlying dynamics involve the Pacific–South America (PSA) teleconnection pattern triggered by Niño 4 SSTs and mediated through wave–mean flow interactions. During boreal winter, warm SSTs in the Niño 4 region enhance convection near the dateline, exciting a Rossby wave train that propagates poleward and eastward across the Southern Hemisphere. This wave activity generates a positive geopotential height anomaly over the southeastern South Pacific and a negative anomaly over the South Atlantic, reinforcing the climatological wave-1 ridge and trough structure. As the seasonal transition into austral summer and winter progresses, the Antarctic stratospheric circulation shifts toward a more westerly regime, creating favorable conditions for planetary waves into the polar stratosphere. The convergence of Eliassen–Palm (E–P) fluxes, followed by wave breaking, induces stratospheric warming and a deceleration of the SPV.

It was also found that warm SSTs in the South Pacific and sea-ice loss over the Amundsen and Ross Seas can reinforce the mid and high latitudes zonal wave train through sea–air interactions. Specially, PSA teleconnection associated with Niño 4 warming drives ocean heat uptake and rising SSTs in the southeast Pacific from January-March to April-June. With progression of seasons, this remote forcing weakens during the June-September, a local sea-air feedback becomes dominant, persistent warm waters accelerate sea-ice melt, and the subsequent oceanic heat release sustains the atmospheric high pressure anomaly, thereby strengthening the planetary wave anomaly.

Furthermore, stronger planetary wave anomalies induced by warm Niño 4 SSTs were found to play a crucial role in modulating Antarctic ozone transport. These anomalous waves enhance the residual circulation, facilitating the ozone transport from the tropics to the polar stratosphere and leading to elevated ozone concentrations over Antarctica. The increased ozone concentrations enhance ultraviolet absorption, further amplifying stratospheric warming. Simultaneously, a warmer stratosphere inhibits the formation of polar stratospheric clouds (PSCs), thereby suppressing the heterogeneous chemical reactions responsible for ozone depletion and mitigating Antarctic ozone loss (Solomon et al., 2016).

A multivariate regression statistical model was used in this study to determine the linear relationship between stratospheric temperature variations and Niño 4 SST. The Niño 4 index alone accounts for approximately 18 % of the variance in July–September polar stratospheric temperatures. However, when the June PSA index is included as additional factor, the explained variance nearly doubles to 32 %. This highlights the combined importance of both tropical forcing and mid–latitude atmospheric responses in stratospheric temperature variability. Nonetheless, a substantial portion of stratospheric variability remains unexplained. This reflects the influence of atmospheric internal dynamics, as well as contributions from other drivers such as the Quasi–Biennial Oscillation (QBO), solar activity, and mid–latitude tropospheric wave sources. Additional factors may be identified through a range of approaches, including numerical modeling, machine learning, and causal inference.

Code and data availability.

The ERA5 reanalysis data are available from the European Centre for Medium–Range Weather Forecasts at Hersbach et al. (2023). Niño 4 index came from National Oceanic and Atmospheric Administration (https://psl.noaa.gov/data/timeseries/month/DS/Nino4/, https://psl.noaa.gov/data/timeseries/month/DS/Nino3/, and https://psl.noaa.gov/data/timeseries/month/DS/Nino34/). The code used in this article is accessible from the corresponding author.

Author contributions

YZ, ZL, JS, and ZX contributed to the conceptualization of the study. YZ designed the methodology, developed the software, performed the validation, formal analysis, investigation, data curation, and visualization. JS, GL, and ZX were responsible for funding acquisition, project administration, and providing the necessary resources. The work was supervised by ZL, JS, GL, WP, and ZX. YZ prepared the original manuscript with contributions from ZL, JS, WP, and ZX. All authors contributed to the review and editing of the final manuscript.

Competing interests

The contact author has declared that none of the authors has any competing interests.

Acknowledgments

The research was supported by the National Natural Science Foundation of China (42394123 and 42394122), “Transforming Climate Action” program (TCA-LRP-20240B-1.1-WP6JS) led by Dalhousie University, Canada, Natural Sciences and Engineering Research Council of Canada to JS (NSERC, Grant NOs: 217081), and the China Scholarship Council (CSC, 202306340119). We also appreciate all the support provided by the Department of Oceanography, Dalhousie University.

Financial support

This research was supported by the National Natural Science Foundation of China (42394123 and 42394122), the “Transforming Climate Action” program (TCA-LRP-20240B-1.1-WP6JS), Natural Sciences and Engineering Research Council of Canada to JS (NSERC, Grant NOs: 217081), and the China Scholarship Council (CSC, 202306340119), Gansu Provincial Natural Science Foundation (25JRRA323).

References

Albers, J.R. and Birner, T.: Vortex Preconditioning due to Planetary and Gravity Waves prior to Sudden Stratospheric Warmings, Journal of the Atmospheric Sciences, 71, 4028–4054, https://doi.org/10.1175/jas-d-14-0026.1, 2014.

Alexander, M.A., Bladé, I., Newman, M., Lanzante, J. R., Lau, N. C., and Scott, J. D.: The Atmospheric Bridge: The Influence of ENSO Teleconnections on Air–Sea Interaction over the Global Oceans, Journal of Climate, 15, 2205–2231, https://doi.org/10.1175/1520-0442(2002)015<2205:tabtio>2.0.co;2, 2002.

Andrews, D. G. and Mcintyre, M. E.: An exact theory of nonlinear waves on a Lagrangian-mean flow, Journal of Fluid Mechanics, 89, 609–646, https://doi.org/10.1017/s0022112078002773, 1978.

Andrews, D. G. and McIntyre, M. E.: Planetary Waves in Horizontal and Vertical Shear: The Generalized Eliassen-Palm Relation and the Mean Zonal Acceleration, Journal of the Atmospheric Sciences, 33, 2031–2048, https://doi.org/10.1175/1520-0469(1976)033<2031:pwihav>2.0.co;2, 1976.

Andrews, D. G., Holton, J. R., and Leovy, C. B.: Middle atmosphere dynamics, Academic Press, 115, 421–422, https://doi.org/10.1002/qj.49711548612, 1987.

Baldwin, M. P. and Dunkerton, T. J.: Stratospheric Harbingers of Anomalous Weather Regimes, Science, 294, 581–584, https://doi.org/10.1126/science.1063315, 2001.

Baldwin, M. P., Ayarzagüena, B., Birner, T., Butchart, N., Butler, A. H., Charlton ‐ Perez, AndrewJ., Domeisen, DanielaI. V., Garfinkel, ChaimI., Garny, H., Gerber, EdwinP., Hegglin, MichaelaI., Langematz, U., and Pedatella, NicholasM.: Sudden Stratospheric Warmings, Reviews of Geophysics, 59, https://doi.org/10.1029/2020rg000708, 2021.

Bamston, A. G., Chelliah, M., and Goldenberg, S. B.: Documentation of a highly ENSO ‐ related sst region in the equatorial pacific: Research note, Atmosphere-Ocean, 35, 367 ‐ 383, https://doi.org/10.1080/07055900.1997.9649597, 1997.

Barriopedro, D. and Calvo, N.: On the Relationship between ENSO, Stratospheric Sudden Warmings, and Blocking, Journal of Climate, 27, 4704–4720, https://doi.org/10.1175/jcli-d-13-00770.1, 2014.

Butler, A. H. and Polvani, L. M.: El Niño, La Niña, and stratospheric sudden warmings: A reevaluation in light of the observational record, Geophysical Research Letters, 38, n/a-n/a, https://doi.org/10.1029/2011gl048084, 2011.

Domeisen, D. I. V., Garfinkel, C. I., and Butler, A. H.: The Teleconnection of El Niño Southern Oscillation to the Stratosphere, Reviews of Geophysics, 57, 5–47, https://doi.org/10.1029/2018rg000596, 2019.

Esler, J. G., Polvani, L. M., and Scott, R. K.: The Antarctic stratospheric sudden warming of 2002: A self ‐ tuned resonance?, Geophysical Research Letters, 33, https://doi.org/10.1029/2006gl026034, 2006.

Evtushevsky, O. M., Kravchenko, V. O., Hood, L. L., and Milinevsky, G. P.: Teleconnection between the central tropical Pacific and the Antarctic stratosphere: spatial patterns and time lags, Climate Dynamics, 44, 1841–1855, https://doi.org/10.1007/s00382-014-2375-2, 2015.

Fogt, R. L., Bromwich, DavidH., and Hines, KeithM.: Understanding the SAM influence on the South Pacific ENSO teleconnection, Climate Dynamics, 36, 1555–1576, https://doi.org/10.1007/s00382-010-0905-0, 2011.

Garfinkel, C. I. and Hartmann, D. L.: Different ENSO teleconnections and their effects on the stratospheric polar vortex, Journal of Geophysical Research: Atmospheres, 113, https://doi.org/10.1029/2008jd009920, 2008.

Grassi, B., Redaelli, G., and Visconti, G.: Tropical SST Preconditioning of the SH Polar Vortex during Winter 2002, Journal of Climate, 21, 5295–5303, https://doi.org/10.1175/2008jcli2136.1, 2008.

Hersbach, H., Bell, B., Berrisford, P., Biavati, G., Horányi, A., Muñoz Sabater, J., Nicolas, J., Peubey, C., Radu, R., Rozum, I., Schepers, D., Simmons, A., Soci, C., Dee, D., and Thépaut, J.-N.: ERA5 hourly data on pressure levels from 1940 to present, Copernicus Climate Change Service (C3S) Climate Data Store (CDS), Dataset, https://doi.org/10.24381/cds.bd0915c6, 2023a.

Hersbach, H., Bell, B., Berrisford, P., Biavati, G., Horányi, A., Muñoz Sabater, J., Nicolas, J., Peubey, C., Radu, R., Rozum, I., Schepers, D., Simmons, A., Soci, C., Dee, D., and Thépaut, J.-N.: ERA5 hourly data on single levels from 1940 to present, Copernicus Climate Change Service (C3S) Climate Data Store (CDS), Dataset, https://doi.org/10.24381/cds.adbb2d47, 2023b.

Hu, Y. and Fu, Q.: Stratospheric warming in Southern Hemisphere high latitudes since 1979, Atmospheric Chemistry and Physics, 9, 4329–4340, https://doi.org/10.5194/acp-9-4329-2009, 2010.

Hurwitz, M. M., Newman, P. A., Oman, L. D., and Molod, A. M.: Response of the Antarctic Stratosphere to Two Types of El Niño Events, Journal of the Atmospheric Sciences, 68, 812–822, https://doi.org/10.1175/2011jas3606.1, 2011a.

Hurwitz, M. M., Song, I.-S., Oman, L. D., Newman, P. A., Molod, A. M., Frith, S. M., and Nielsen, J. E.: Response of the Antarctic stratosphere to warm pool El Niño Events in the GEOS CCM, Atmospheric Chemistry and Physics, 11, 9659–9669, https://doi.org/10.5194/acp-11-9659-2011, 2011b.

Ineson, S. and Scaife, A. A.: The role of the stratosphere in the European climate response to El Niño, Nature Geoscience, 2, 32–36, https://doi.org/10.1038/ngeo381, 2009.

Karpetchko, A., Kyrö, E., and Knudsen, B. M.: Arctic and Antarctic polar vortices 1957 ‐ 2002 as seen from the ERA ‐ 40 reanalyses, Journal of Geophysical Research: Atmospheres, 110, https://doi.org/10.1029/2005jd006113, 2005.

Kim, B.-M., Choi, H., Kim, S.-J., and Choi, W.: Amplitude-dependent relationship between the Southern Annular Mode and the El Niño Southern Oscillation in austral summer, Asia-Pacific Journal of Atmospheric Sciences, 53, 85–100, https://doi.org/10.1007/s13143-017-0007-6, 2017.

Kuroda, Y., Deushi, M., and Shibata, K.: Role of solar activity in the troposphere ‐ stratosphere coupling in the Southern Hemisphere winter, Geophysical Research Letters, 34, https://doi.org/10.1029/2007gl030983, 2007.

L'Heureux, M. L. and Thompson, D. W. J.: Observed Relationships between the El Niño–Southern Oscillation and the Extratropical Zonal-Mean Circulation, Journal of Climate, 19, 276–287, https://doi.org/10.1175/jcli3617.1, 2006.

Laat, A. T. J., and Weele, M. V: The 2010 Antarctic ozone hole: Observed reduction in ozone destruction by minor sudden stratospheric warmings, Scientific Reports, 1, https://doi.org/10.1038/srep00038, 2011.

Lim, E. ‐ P., Hendon, H. H., and Thompson, D. W. J.: Seasonal Evolution of Stratosphere ‐ Troposphere Coupling in the Southern Hemisphere and Implications for the Predictability of Surface Climate, Journal of Geophysical Research: Atmospheres, 123, 12,002-12,016, https://doi.org/10.1029/2018jd029321, 2018.

Lim, E., Zhou, L., Young, G., Abhik, S., Rudeva, I., Hope, P., Wheeler, M. C., Arblaster, J. M., Hendon, H. H., Manney, G., Son, S., Oh, J., and Garreaud, R. D.: Predictability of the 2020 Strong Vortex in the Antarctic Stratosphere and the Role of Ozone, Journal of Geophysical Research: Atmospheres, 129, https://doi.org/10.1029/2024jd040820, 2024.

Lin, J. and Qian, T.: Impacts of the ENSO Lifecycle on Stratospheric Ozone and Temperature, Geophysical Research Letters, 46, 10646–10658, https://doi.org/10.1029/2019gl083697, 2019.

Lin, P., Fu, Q., and Hartmann, D. L.: Impact of Tropical SST on Stratospheric Planetary Waves in the Southern Hemisphere, Journal of Climate, 25, 5030–5046, https://doi.org/10.1175/jcli-d-11-00378.1, 2012.

Lin, P., Fu, Q., Solomon, S., and Wallace, J. M.: Temperature Trend Patterns in Southern Hemisphere High Latitudes: Novel Indicators of Stratospheric Change, Journal of Climate, 22, 6325–6341, https://doi.org/10.1175/2009jcli2971.1, 2009.

Ma, C., Yang, P., Tan, X., and Bao, M.: Possible Causes of the Occurrence of a Rare Antarctic Sudden Stratospheric Warming in 2019, Atmosphere, 13, 147, https://doi.org/10.3390/atmos13010147, 2022.

Manatsa, D. and Mukwada, G.: A connection from stratospheric ozone to El Niño-Southern Oscillation, Scientific Reports, 7, https://doi.org/10.1038/s41598-017-05111-8, 2017.

Matsuno, T. A Dynamical Model of the Stratospheric Sudden Warming. Journal of the Atmospheric Sciences, 28(8), 1479–1494. https://doi.org/10.1175/1520-0469(1971)028<1479:admots>2.0.co;2, 1971.

McPhaden, M. J., Zebiak, S. E., and Glantz, M. H.: ENSO as an Integrating Concept in Earth Science, Science, 314, 1740–1745, https://doi.org/10.1126/science.1132588, 2006.

Mo, K.C. and Higgins, R. W.: The Pacific–South American Modes and Tropical Convection during the Southern Hemisphere Winter, Monthly Weather Review, 126, 1581–1596, https://doi.org/10.1175/1520-0493(1998)126<1581:tpsama>2.0.co;2, 1998.

Niu, Y., Xie, F., and Wu, S.: ENSO Modoki Impacts on the Interannual Variations of Spring Antarctic Stratospheric Ozone, Journal of Climate, 36, 5641–5658, https://doi.org/10.1175/jcli-d-22-0826.1, 2023.

O'Neill, A., and C. Youngblut,: Stratospheric warmings diagnosed using the transformed Eulerian-mean equations and the effect of the mean state on wave propagation. Journal of the Atmospheric Sciences, 39, 1370 – 1386, doi:10.1175/1520-0469(1982)039,1370: SWDUTT.2.0.CO;2. 1982.

Polvani, L. M., Sun, L., Butler, A. H., Richter, J. H., and Deser, C.: Distinguishing Stratospheric Sudden Warmings from ENSO as Key Drivers of Wintertime Climate Variability over the North Atlantic and Eurasia, Journal of Climate, 30, 1959–1969, https://doi.org/10.1175/jcli-d-16-0277.1, 2017.

Rao, J., Garfinkel, C. I., Ren, R., Wu, T., and Lu, Y.: Southern Hemisphere Response to the Quasi-Biennial Oscillation in the CMIP5/6 Models, Journal of Climate, 36, 2603–2623, https://doi.org/10.1175/jcli-d-22-0675.1, 2023.

Rayner, N. A., Parker, D. E., Horton, E. B., Folland, C. K., Alexander, L. V., Rowell, D. P., Kent, E. C., and Kaplan, A.: Global analyses of sea surface temperature, sea ice, and night marine air temperature since the late nineteenth century, Journal of Geophysical Research: Atmospheres, 108, https://doi.org/10.1029/2002jd002670, 2003.

Rea, D., Elsbury, D., Butler, A.H., Sun, L., Peings, Y., and Magnusdottir, G.: Interannual Influence of Antarctic Sea Ice on Southern Hemisphere Stratosphere-Troposphere Coupling, Geophysical Research Letters, 51, https://doi.org/10.1029/2023gl107478, 2024.

Shen, X., Wang, L., and Osprey, S.: Tropospheric Forcing of the 2019 Antarctic Sudden Stratospheric Warming, Geophysical Research Letters, 47, https://doi.org/10.1029/2020gl089343, 2020.

Silvestri, G. and Vera, C.: Nonstationary Impacts of the Southern Annular Mode on Southern Hemisphere Climate, Journal of Climate, 22, 6142–6148, https://doi.org/10.1175/2009jcli3036.1, 2009.

Singh, A. K. and Bhargawa, A.: Atmospheric burden of ozone depleting substances (ODSs) and forecasting ozone layer recovery, Atmospheric Pollution Research, 10, 802–807, https://doi.org/10.1016/j.apr.2018.12.008, 2019.

Solomon, S., Ivy, D. J., Kinnison, D., Mills, M. J., Neely, R. R., and Schmidt, A.: Emergence of healing in the Antarctic ozone layer, Science, 353, 269–274, https://doi.org/10.1126/science.aae0061, 2016.

Song, K. and Son, S.-W.: Revisiting the ENSO–SSW Relationship, Journal of Climate, 31, 2133–2143, https://doi.org/10.1175/jcli-d-17-0078.1, 2018.

Song, J., Zhang, J., Du, S., Xu, M., and Zhao, S.: Impact of Early Winter Antarctic Sea Ice Reduction on Antarctic Stratospheric Polar Vortex, Journal of Geophysical Research: Atmospheres, 130, https://doi.org/10.1029/2024jd041831, 2025.

Stone, K. A., Solomon, S., Thompson, D. W. J., Kinnison, D. E., and Fyfe, J. C.: On the Southern Hemisphere stratospheric response to ENSO and its impacts on tropospheric circulation, Journal of Climate, 35, 1963–1981, https://doi.org/10.1175/jcli-d-21-0250.1, 2022.

Sun, L., Deser, C., and Tomas, R.A.: Mechanisms of Stratospheric and Tropospheric Circulation

Response to Projected Arctic Sea Ice Loss, Journal of Climate, 28, 7824 – 7845, https://doi.org/10.1175/jcli-d-15-0169.1, 2015.

Takaya, K. and Nakamura, H.: A Formulation of a Phase-Independent Wave-Activity Flux for Stationary and Migratory Quasigeostrophic Eddies on a Zonally Varying Basic Flow, Journal of the Atmospheric Sciences, 58, 608–627, https://doi.org/10.1175/1520-0469(2001)058<0608:afoapi>2.0.co;2, 2001.

Thompson, D. W. J. and Solomon, S.: Interpretation of Recent Southern Hemisphere Climate Change, Science, 296, 895–899, https://doi.org/10.1126/science.1069270, 2002.

Thompson, D. W. J., Baldwin, M. P., and Solomon, S.: Stratosphere–Troposphere Coupling in the Southern Hemisphere, Journal of the Atmospheric Sciences, 62, 708–715, https://doi.org/10.1175/jas-3321.1, 2005.

Thompson, D. W. J., Solomon, S., Kushner, P. J., England, M. H., Grise, K. M., and Karoly, D. J.: Signatures of the Antarctic ozone hole in Southern Hemisphere surface climate change, Nature Geoscience, 4, 741–749, https://doi.org/10.1038/ngeo1296, 2011.

Trenberth, K. E.: The Definition of El Niño, Bulletin of the American Meteorological Society, 78, 2771 – 2777, https://doi.org/10.1175/1520-0477(1997)078<2771:tdoeno>2.0.co;2, 1997.

Wang, C.: A review of ENSO theories, National Science Review, 5, 813–825, https://doi.org/10.1093/nsr/nwy104, 2018.

Wang, Z., Zhang, J., Zhao, S., and Li, D.: The joint effect of mid-latitude winds and the westerly quasi-biennial oscillation phase on the Antarctic stratospheric polar vortex and ozone, Atmospheric Chemistry and Physics, 25, 3465–3480, https://doi.org/10.5194/acp-25-3465-2025, 2025.

Yang, C., Li, T., Dou, X., and Xue, X.: Signal of central Pacific El Niño in the Southern Hemispheric stratosphere during austral spring, Journal of Geophysical Research: Atmospheres, 120, https://doi.org/10.1002/2015jd023486, 2015.

Zhang, R., Zhou, W., Tian, W., Zhang, Y., Liu, Z., and Cheung, P. K. Y.: Changes in the Relationship between ENSO and the Winter Arctic Stratospheric Polar Vortex in Recent Decades, Journal of Climate, 35, 5399–5414, https://doi.org/10.1175/jcli-d-21-0924.1, 2022.

Zi, Y., Long, Z., Sheng, J., Lu, G., Perrie, W., and Xiao, Z.: The Sudden Stratospheric Warming Events in the Antarctic in 2024, Geophysical Research Letters, 52, https://doi.org/10.1029/2025gl115257, 2025.

Zubiaurre, I. and Calvo, N.: The El Niño–Southern Oscillation (ENSO) Modoki signal in the stratosphere, Journal of Geophysical Research: Atmospheres, 117, https://doi.org/10.1029/2011jd016690, 2012.